

Seasonality of Internal Tides in the Strait of Hormuz: Observations and Modeling



Key Points:

- Mooring data from the Strait of Hormuz show strong seasonal variations in internal tides, with enhanced diurnal internal tides during winter
- Modeled barotropic-to-baroclinic conversion and flux estimates show that topography near the mooring location is the generation source
- In winter, stratification and tidal forcing favor diurnal internal tide excitation, while other seasons also support semidiurnal tides

Supporting Information:

Supporting Information may be found in the online version of this article.

Correspondence to:

M. R. Al Shehhi,
maryamr.alshhhi@ku.ac.ae

Citation:

Subeesh, M. P., Song, H., Addad, Y., Scott, J. R., Marshall, J., & Al Shehhi, M. R. (2025). Seasonality of internal tides in the Strait of Hormuz: Observations and modeling. *Journal of Geophysical Research: Oceans*, 130, e2024JC021007. <https://doi.org/10.1029/2024JC021007>

Received 10 FEB 2024

Accepted 23 FEB 2025

Author Contributions:

Conceptualization: M. P. Subeesh, Hajoon Song, Yacine Addad, Jeffery R. Scott, John Marshall, Maryam R. Al Shehhi

Data curation: M. P. Subeesh

Formal analysis: M. P. Subeesh,

Hajoon Song, Jeffery R. Scott

Funding acquisition: John Marshall,

Maryam R. Al Shehhi

Investigation: M. P. Subeesh,

Hajoon Song

Methodology: M. P. Subeesh

Project administration: Maryam R. Al

Shehhi

M. P. Subeesh^{1,2,3} , Hajoon Song^{4,5} , Yacine Addad⁶ , Jeffery R. Scott⁷ , John Marshall⁷, and Maryam R. Al Shehhi¹ 

¹Department of Civil and Environmental Engineering, Khalifa University of Science and Technology, Abu Dhabi, United Arab Emirates, ²MARUM—Center for Marine Environmental Science, University of Bremen, Bremen, Germany, ³Institute of Environmental Physics, University of Bremen, Bremen, Germany, ⁴Department of Atmospheric Sciences, Yonsei University, Seoul, Korea, ⁵Division of Environmental Science & Engineering, Pohang University of Science and Technology, Pohang, Republic of Korea, ⁶Department of Nuclear Engineering, Khalifa University of Science and Technology, Abu Dhabi, United Arab Emirates, ⁷Earth, Atmospheric and Planetary Science Department, Massachusetts Institute of Technology, Cambridge, MA, USA

Abstract The seasonality of internal tides in shallow seas is primarily controlled by changes in stratification. This study explores how semidiurnal and diurnal internal tides respond differently to seasonal stratification, using mooring observations and numerical modeling in the Strait of Hormuz, the gateway for hypersaline Arabian Gulf waters. Semidiurnal internal tides are weak during winter, which is attributed to relatively weak stratification, whereas diurnal internal tides are enhanced. In the remaining seasons, internal tides are strong in both bands. Estimates of energy flux and barotropic-to-baroclinic conversion rates from observations and modeling show a likely generation site near the mooring location. In winter, this generation site turns subcritical at semidiurnal frequencies and supercritical at diurnal frequencies. In addition, barotropic tides show significant amplification at the diurnal frequency during winter. Thus, supercritical topography along with strong barotropic tidal forcing enhances the diurnal internal tides. In the remaining seasons, the topography becomes either critical or supercritical for the semidiurnal frequency and supercritical for the diurnal frequency, resulting in strong internal tide generation. The results of our model show that low-frequency currents significantly influence stratification in the strait, thus playing a crucial role in modulating internal tides. In turn, vertical mixing orchestrated by those tides may be important in setting water mass transformation rates, stratification, and exchange through the strait.

Plain Language Summary The interaction of barotropic (surface) tides with topography in a stratified ocean generates internal tides that can induce mixing and hence modify the water masses. Here we explore how the two major frequencies of internal tides—diurnal and semidiurnal, once and twice a day, respectively—respond to the seasonal variation of stratification in the Strait of Hormuz. Observations show significant internal tide activity at both frequencies, but with contrasting seasonal variations. In winter, semidiurnal internal tides are weak, and diurnal tides are strong. In other seasons, both frequency bands are active. A model is used to explore the generation site, propagation, dissipation, and seasonal modulation of these tides. They are generated by barotropic tides flowing over a topographic feature close to the mooring. In winter, stratification is such that the diurnal internal tide is favored. In addition, barotropic tides are strong in winter compared to other seasons, which further intensify the diurnal internal tides. The stratification and barotropic tides in the remaining seasons favor the internal tides in both bands.

1. Introduction

Internal tides in the ocean are mainly generated over topographic features such as sea mounts, shelf-breaks and continental slopes, when the barotropic tides interact with bottom topography in the presence of stratification. A part of the internal tide is dissipated locally at the generation site, while the remainder propagates and can dissipate far away. Internal tides are one of the main sources of mechanical energy in the interior ocean, leading to mixing of the water masses in the deep ocean (Munk & Wunsch, 1998). In shallow waters, turbulent mixing associated with internal tides, for example, causes upward transport of nutrients from subsurface waters, increasing biological productivity (Sharples et al., 2009). Turbulent mixing at the bottom of continental margins driven by internal tides can lead to sediment resuspension, mass, and momentum transport (Masunaga

© 2025. The Author(s).

This is an open access article under the terms of the [Creative Commons Attribution-NonCommercial-NoDerivs License](https://creativecommons.org/licenses/by/4.0/), which permits use and distribution in any medium, provided the original work is properly cited, the use is non-commercial and no modifications or adaptations are made.

Resources: Maryam R. Al Shehhi
Software: M. P. Subeesh
Supervision: John Marshall, Maryam R. Al Shehhi
Validation: M. P. Subeesh
Visualization: M. P. Subeesh
Writing – original draft: M. P. Subeesh
Writing – review & editing: Hajoon Song, Yacine Addad, Jeffery R. Scott, John Marshall, Maryam R. Al Shehhi

et al., 2017). Understanding and mapping internal tide generation sites and the propagation and dissipation of those tides in deep and shallow parts of the ocean are therefore critically important.

The generation and propagation of internal tides are sensitive to ocean stratification and are therefore strongly modulated by ocean environments. Seasonally varying internal tides have been observed in a number of studies on continental shelves (Eich et al., 2004; Guo et al., 2012; Jithin et al., 2017; Subeesh et al., 2013), continental slopes (Subeesh & Unnikrishnan, 2016), and the deep ocean (Kaur et al., 2024; Zhao, 2021). Studies have shown that strong stratification enhances internal tide activity in the summer relative to winter. For example, Zhao and Qiu (2023) reported strong (weak) semidiurnal internal tides in the Luzon Strait during summer (winter) using satellite observations. Gerkema et al. (2004) observed a 15% of increase in barotropic to baroclinic conversion in the Bay of Biscay during summer relative to winter. In addition to stratification, seasonal changes in barotropic tides can also lead to seasonal variations in internal tides. For example, Yan et al. (2020) demonstrated that the intensification of diurnal internal tides in summer is linked to stronger barotropic tides combined with enhanced stratification. Similarly, Liu et al. (2015) observed enhanced diurnal internal tides in winter, attributed to seasonal variation in barotropic tides. However, there remains limited understanding or observations of the differing response of semidiurnal and diurnal internal tides to seasonal variations of barotropic tides and stratification.

In this study, we explore the interplay of tides, topography, and stratification, and the seasonal cycle in the Strait of Hormuz (SH), which separates the Arabian Gulf (AG) from the Sea of Oman. This is of great interest, not least because the exchange between the inner Gulf and the outer Sea is likely sensitive to mixing processes associated with the tide (Salim et al., 2024). The AG is a shallow inland sea, approximately 1,000 km long, 250–300 km wide, with a depth of 50–100 m (Figure 1). The AG has an arid climate with very high evaporation rates of ~2 m per year that exceed the fresh water input of ~0.15 m per year (Johns et al., 2003). This results in the formation of one of the most saline seas (>41 psu) on Earth. This salty water spreads out into the northern Indian Ocean, affecting its hydrography and circulation (Jain et al., 2016). The SH acts as the gateway from the AG to the Sea of Oman. It is roughly 160 km long, 40–100 km wide and deep at its center, reaching ~110 m, but with complex bathymetric features (Pous et al., 2004). The waters mainly sink along the southern coast, near the United Arab Emirates, and flow out into the Sea of Oman in the deepest part of the SH. In compensation, water flows into the AG primarily in the upper water column.

The AG is characterized by seasonal variations in circulation, water mass distribution, and stratification. In summer (June–September), strong short-wave fluxes are absorbed by low saline surface waters from the Sea of Oman (Kämpf & Sadrinasab, 2006), leading to strong vertical stratification (Al-Ansari et al., 2022). In winter (December–February), the winds mix the water column and weaken the stratification (Al Azhar et al., 2016). The dense waters that form in winter in the northern Gulf region spread south throughout the year (Swift & Bower, 2003), with a maximum surface salinity exceeding 40 psu (Johns et al., 2003). The shallow southeastern shelves are a primary dense water source, spilling into the deepest part of the Gulf and then out through the SH. The stratification of SH waters is strongly modulated by this seasonally varying outflow (Johns et al., 2003), along with the seasonal variation of air-sea fluxes. This broad cycle is captured in state-of-the-art ocean models, for example, the one described by Al-Shehhi et al. (2021) and employed here.

The currents in the SH are dominated by barotropic (depth-independent) tides (Johns et al., 2003). Observations reveal barotropic tides at both the semidiurnal and diurnal frequencies (Johns et al., 2003). These tidal currents flow over the complex bottom, and so can be expected to generate internal tides, providing a route to mixing of the water column. Although there have been no detailed studies of internal tides in the SH, satellite observations suggest significant internal tide activity (Andi et al., 2020; Ma et al., 2021). The SH is thus interesting for two main reasons: first, the stratification is modulated by seasonally varying, low-frequency currents, and second, there are both semidiurnal and diurnal tides. Focusing on this region provides an opportunity to study how semidiurnal and diurnal internal tides respond to seasonal stratification changes modulated by low-frequency background currents under similar barotropic forcing. As noted above, this is the motivation and theme of the present study.

We used long-term mooring observations of currents and hydrography in the SH to document the basic characteristics of internal tides, their magnitude, vertical structure, propagation, and seasonality. Since mooring observations restrict our analysis to a single point, we use a high-resolution Massachusetts Institute of Technology General Circulation Model (MITgcm) to identify internal tide generation sites and affecting factors. The model is also used to address the role of low-frequency, bottom-density currents in modulating the stratification, and thereby seasonality of the internal tide.

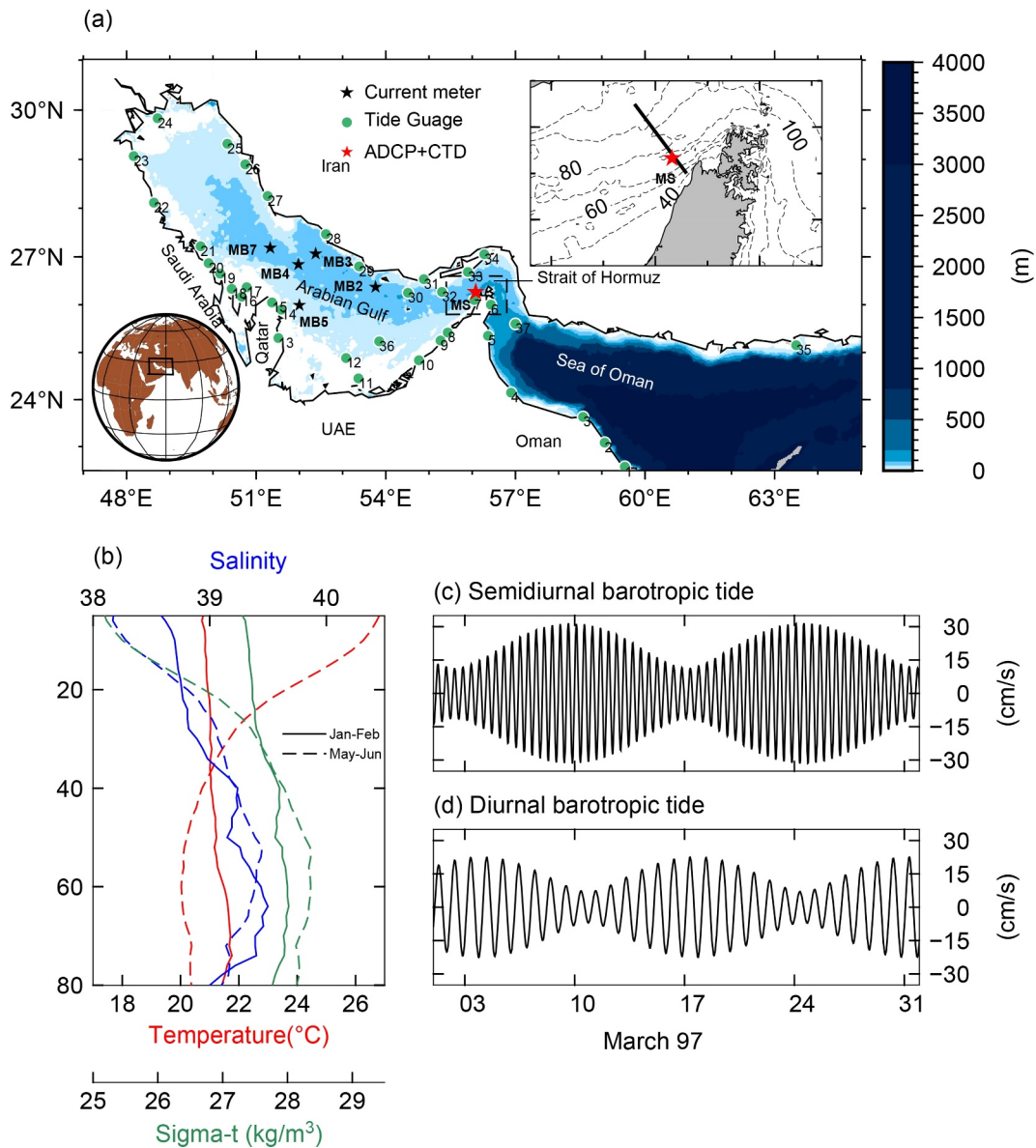


Figure 1. (a) Bathymetric relief of the model domain, encompassing the Arabian Gulf, Strait of Hormuz and the Sea of Oman. The dashed square shows our domain of interest and is expanded in the top right corner. The position of the transect in the SH is marked in black and the mooring location is marked with a red star. Current meter mooring locations in the inner Gulf are marked by black stars and set out in Table A1. The green circles represent numbered tide gauge locations along the coast. (b) Spatial average of temperature, salinity and density from the Master Oceanographic Observations Data set data over the AG: bold (dashed) line for January–February (May–June). (c)–(d) Eastward components of the semidiurnal and diurnal barotropic tidal currents at the mooring location in the strait.

Our paper is organized as follows. Section 2 describes the data used and the configuration of the MITgcm model for the AG. Section 3 presents observations of internal tides in the SH using mooring data. In Section 4, the model is evaluated against hydrography and mooring data, followed by in-depth analyzes of the model results. Finally, Section 5 concludes with a discussion of our key findings.

2. Data and Methods

2.1. Mooring Observations

Mooring observations of currents, temperature, and salinity (Johns et al., 2003) from SH (Figure 1) are used to investigate the seasonal variability of internal tides in the region. The water depth at the moorings is ~ 110 m. Two moorings were deployed approximately 400 m apart. The first consisted of an upward looking 150 kHz

Acoustic Doppler Current meter Profiler (ADCP) at 15 m above the bottom, with a current meter mounted on the mooring at 10 m above the bottom. In the second, SeaCat sensors placed at depths of 20, 40, 60, 80, and 100 m were used to measure temperature, salinity and pressure. In addition, temperature sensors were also placed at depths of 30, 50, 70, and 90 m. Measurements were taken every 30 min. The moorings were first deployed in December 1996 and then serviced and redeployed in July 1997. The time series measurements cover 15 months, from December 1996 to March 1998. Although most instruments recorded complete data sets throughout this period, ADCPs stopped working after 4–5 months in both deployments. ADCP record was thus only available from 15 December/1996 to 03 December/1997, with a 2.5-month gap from 9 May/1997 to 29 July/1997. A comprehensive description of the mooring data is given in Johns et al. (2003). The current meter data at 100 m are combined with the ADCP data to obtain the maximum depth coverage. We then vertically averaged the currents to obtain the barotropic current, and the residual yielded the baroclinic current. The semidiurnal and diurnal tidal components are extracted from the barotropic and baroclinic currents using a third-order Butterworth bandpass filter, and harmonic analysis using the Tidal Analysis Software Kit package.

Various other data sets were used to assess the performance of the model and its representation of tides (see Section 4): 37 tide gauge stations distributed over the AG and the Sea of Oman (Figure 1) and 5 moored current meters from the central AG from the *Mt Mitchell* expedition (Michael Reynolds, 1993). Table A1 details the mooring locations, time period and frequency of the measurements of both inner AG moorings and the main mooring in the SH.

To compare seasonal means of temperature and salinity, we used historical observations from the Master Oceanographic Observations Data set (MOODS) (Alessi et al., 1999) available for AG and the Sea of Oman. MOODS data span the period 1940–1990 and are sparsely distributed in time and space in the region (Al-Shehhi et al., 2021). Hence, we selected 18 boxes along the AG by following Swift and Bower (2003), and prepared a seasonal climatology for each box. We used subsets of 2 months for each season to compute seasonal climatology. January–February for winter, March–April for spring, and July–August for summer.

2.2. Numerical Model Configuration Using MITgcm

A three-dimensional high-resolution regional hydrodynamic model, the MITgcm (Marshall et al., 1997), configured for the AG, is used to simulate internal tides. The model is used to identify major internal tide generation sites in the SH and to decipher their propagation, dissipation, and seasonal variation.

The model domain comprises the Sea of Oman and AG (23.2°N to 30.7°N and 47.3°E to 62.3°E). The bathymetry of the model is prepared by combining digitized soundings from HDNO-GUNIO charts (Figure S1 in Supporting Information S1) and the Smith and Sandwell Global Topography resolution of 2 arc min (Smith & Sandwell, 1997). The horizontal resolution is 1/48°, or approximately 2.5 km. We employ 83 z coordinate layers vertically, with a gradual increase in layer thickness from 1 to 250 m to account for bottom depths up to 4,000 m. The thickness vary from ~O (1–2 m) in the upper 10 m, ~O (2–10 m) for the upper 100 m, to ~O (10–200 m) for the subsurface to deeper depths in the Sea of Oman (Figure 1). The initial 22 layers are dedicated to covering the upper 100 m depth, providing sufficient vertical resolution for the inner AG and SH. The model is spun up for the period 01 January 1994–01 December 1996, and the period 01 December 1996–31 December 1997 is used in the analysis.

Eastern and southern boundaries of the model domain are open, where the Orlanski (1976) radiation boundary conditions are used. The temperature, salinity, horizontal velocity, and sea surface height data for the initial and lateral boundary conditions are obtained from the high-resolution (1/12° in horizontal, 40 vertical levels) Hybrid Coordinate Ocean Model and the Navy Coupled Ocean Data Assimilation (HYCOM + NCODA) global analysis (GLBv0.08/expt_53.X) data (<https://www.hycom.org/data/glbv0pt08>). The three-hourly data are averaged daily and are interpolated to horizontal and vertical model grids. The tidal forcing along the open boundaries for the 10 major tidal constituents (M_2 , S_2 , N_2 , K_1 , O_1 , K_1 , P_1 , Q_1 , M_f and M_m) are obtained from the OSU Tidal Inversion Software Arabian sea regional barotropic model (Egbert & Erofeeva, 2002) (<https://www.tpxo.net/regional>). The amplitudes and phases of the eastward and northward components of tidal currents are given along the eastern and southern boundaries, respectively.

Table 1
Parameters of the Barotropic Tidal Ellipses of Four Tidal Constituents in the Strait of Hormuz Computed Using Vertically Averaged Currents From Mooring Data for the Period 15 December 1996–10 May 1997

	M ₂	S ₂	K ₁	O ₁
Semimajor axis (cm/s)	25.00	10.00	27.50	9.78
Semiminor axis (cm/s)	0.03	0.11	0.37	0.39
Phase (°)	59.43	70.62	28.56	22.29
Inclination (°)	36.80	36.30	219.20	217.20

The model is forced by atmospheric data from the European Center for Medium-Range Weather Forecasts (ECMWF), including components of 10 m wind velocity, sea level pressure, 2 m air temperature, and specific humidity, precipitation, and short-wave and long-wave radiation. The horizontal resolution of the atmospheric data is roughly 31 km, and the temporal resolution is 1 hour. Air-sea fluxes are estimated using bulk flux formulations (Fairall et al., 2003). The discharge from the Shatt Al-Arab, Mand, Hindijan and Hilieh rivers is provided monthly (Al-Shehhi et al., 2021; Salim et al., 2024). The horizontal mixing on the subgrid scale in the model is parameterized using a modified Leith viscosity (Leith, 1996), with a horizontal background viscosity set to 10 m²/s. Vertical mixing is parameterized

using the K profile parameterization scheme (KPP) (Large et al., 1994). The background vertical viscosity is set to 10⁻⁵ m²/s and a bottom drag coefficient of 2.5 × 10⁻³ is employed.

3. Observations of Internal Tides in the Strait of Hormuz

3.1. Characteristics of the Barotropic and Internal Tides

Barotropic tidal currents in the semidiurnal and diurnal bands extracted from the SH mooring data are shown in Figures 1c and 1d respectively. Both bands are of similar magnitude with significant spring-neap variability. The amplitude of the barotropic tide in the semidiurnal (diurnal) band reaches about 30 cm/s (20 cm/s) during the spring phase. The barotropic tidal ellipse parameters for M₂, S₂, K₁, and O₁—the predominant semidiurnal and diurnal tidal constituents—are shown in Table 1. These parameters are derived by harmonic analysis of the barotropic currents observed from December to May. The semi-major axis of M₂ and K₁ is ~25 cm/s and ~27 cm/s respectively, with slightly higher magnitudes for K₁. The orientation of the M₂ and K₁ ellipses is similar, with maximum currents oriented along the SH axis. Furthermore, the value of the form factor $F = (K_1 + O_1)/(M_2 + S_2)$, estimated using the semi-major axis of the diurnal and semidiurnal tidal currents, is close to 1, showing that the barotropic tidal currents have roughly equal contributions from the diurnal and semidiurnal components.

Earlier studies have shown that barotropic tides can undergo significant seasonal modulation due to changes in stratification, currents, sea level, and meteorological forcing (Devlin et al., 2017; Müller, 2012; Yan et al., 2020). To investigate the seasonal variability of barotropic tides at the mooring location, we conducted a harmonic analysis of barotropic currents separately for each season. We defined December–February as winter, March–May as spring, August–September as summer, and October–November as fall. The semimajor axes of the four tidal constituents for these seasons are presented in Table 2. The orientation of the ellipses remained relatively consistent throughout the seasons for all constituents. For M₂ and S₂, the values of the semi-major axis varied by less than 2 cm/s from season to season, indicating weak seasonal variation. However, K₁ showed significant seasonal variation, with strong currents in winter reaching approximately 30 cm/s. In spring, K₁ decreased by approximately 9 cm/s compared to winter, while in summer and fall, it increased by 3 cm/s and 6 cm/s from the spring-season values, respectively. O₁ also showed seasonal variation, with a minimum in winter and a maximum in spring. These results indicate that the diurnal barotropic forcing varies significantly with season at the mooring location.

The basic characteristics of the internal tides at the mooring location are summarized in Figure 2. Figure 2a shows vertically averaged rotary spectra (Mooers, 1973) of baroclinic currents, computed using baroclinic current observations from December to May, revealing significant internal tides with predominantly clockwise rotation during the observation period. We see elevated power at semidiurnal and diurnal tidal frequencies, with a more energetic diurnal peak. Smaller peaks are also seen at higher harmonics, such as at the M₄ and M₆ frequencies. To understand temporal variability, baroclinic currents are bandpassed using a third-order Butterworth filter with a bandwidth of 0.7f_r – 1.3f_r (where f_r is the frequency of M₂ or K₁). The temporal evolution of baroclinic tides in these bands for December 1996 and March 1997 is illustrated in Figures 2b–2e. The internal tides generate current speeds with amplitudes of 8–12 cm/s in both bands. In December, the semidiurnal internal tides are weak while the diurnal internal tides are strong. In March, both the semidiurnal and diurnal bands are strong. The tendency for opposing flow in the upper and lower water column indicates that the vertical structure of both the semidiurnal and diurnal internal tides is dominated by first-mode signals. This is also evident from observed isotherm

Table 2

Semimajor Axis (cm/s) of Barotropic Tidal Ellipses for Four Tidal Constituents in the Strait of Hormuz, Computed Using Vertically Averaged Currents for Different Seasons

	M ₂	S ₂	K ₁	O ₁
Winter	24.36	9.970	30.80	7.627
Spring	25.95	11.80	21.65	11.49
Summer	25.15	11.91	23.61	11.33
Fall	25.64	12.39	26.37	9.933

displacement (not shown), where the maximum vertical displacement due to internal tide activity occurs at mid-depths. The spring-neap cycle is also evident, with maximum amplitude coinciding with the barotropic spring tide (Figures 1c, 1d, 2d, and 2e). The in-phase relation between the spring-neap cycle of local barotropic forcing and that of the internal tides is suggestive of a potential nearby internal tide generation site. Strong bottom currents are also observed in the diurnal band during December, with values up to 12 cm/s during the spring phase of the barotropic tide.

3.2. Seasonal Variation of Internal Tides

The density difference between the lower (100 m) and upper (20 m) levels of the water column (Figure 2f) obtained from the mooring observations indicates a significant seasonal variation in stratification. The water column is weakly stratified in winter (December–February), moderately stratified in spring (March–May), and strongly stratified in summer (June–September). Stratification begins to weaken in the fall season (October–November). To understand the variation of internal tides associated with this seasonally variable stratification, the horizontal kinetic energy (HKE) integrated in depth for the observation period is plotted (Figure 2f). HKE is computed as follows:

$$HKE = \frac{\rho_0}{2} \int_{-H}^0 \langle \mathbf{u}'^2(z) \rangle dz \quad (1)$$

where ρ_0 is the vertically averaged density and \mathbf{u}' is the eastward and northward components of semidiurnal and diurnal baroclinic velocity. Both bands show significant variation around their temporal mean (dashed lines). The semidiurnal component has a significantly lower energy in the winter months, when the maximum diurnal internal tide energy occurs, about three to six times stronger. As such, the total internal tide is mostly determined by the diurnal band in winter; these maxima occur when the stratification is weak. During the spring season, the semidiurnal internal tides strengthen (as evidenced by occurrence of energetic peaks, generally following the spring-neap cycle), with both bands exhibiting similar magnitudes. During August–November, representative of the summer and fall months, energetic peaks in both bands are found to occur. It is interesting to note that the diurnal internal tides are at their maximum when stratification is weak. One possible reason for this enhancement is the strong barotropic forcing in the diurnal band during winter, as shown in Table 2. In Section 4, we will explore how weak stratification, combined with strong barotropic forcing, contributes to the enhancement of diurnal internal tides using our model simulations.

3.3. Internal Tide Energy Flux Inferred From Mooring Observations

To determine the propagation characteristics of the semidiurnal and diurnal internal tides at the mooring location, we computed the internal tide energy flux using equation,

$$\mathbf{F} = \int_0^H \langle \mathbf{u}' p' \rangle dz \quad (2)$$

and \mathbf{u}' and p' are the horizontal components of the baroclinic tidal currents and pressure respectively. The angle bracket denotes the time average of energy flux over the tidal period (Alford & Zhao, 2007). Baroclinic tidal currents are extracted by setting,

$$\mathbf{u}'(z) = \mathbf{u}(z) - \mathbf{u}_{bt} \quad (3)$$

where \mathbf{u} is the horizontal component of total tidal current and \mathbf{u}_{bt} is the barotropic tidal current ($\mathbf{u}_{bt} = \frac{1}{H} \int_0^H \mathbf{u}(z) dz$).

Baroclinic pressure is calculated using an indirect method following Kunze et al. (2002):

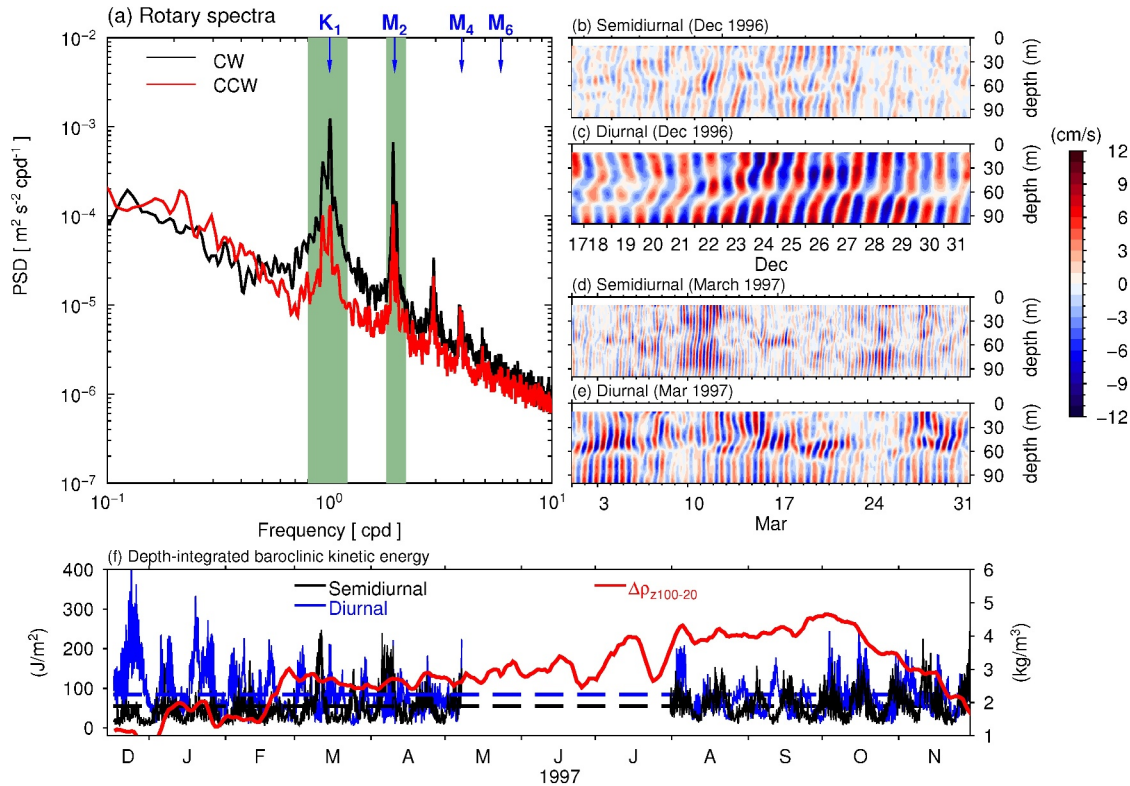


Figure 2. (a) Vertically averaged clockwise (black) and anticlockwise (red) rotary spectra of baroclinic currents obtained from mooring observation. The major tidal frequencies are marked. Depth-time series of the (b)–(e) semidiurnal and diurnal bandpassed internal tidal currents (color scale at the rhs) at the mooring location during December 1996 and March 1997. (f) Time series of semidiurnal (black) and diurnal (blue) kinetic energy (Equation 1) integrated over depth (scale on the lhs). Kinetic energy is estimated using eastward and northward components of bandpassed semidiurnal and diurnal internal tides obtained from mooring data. The dashed lines are the time averages over the record for semidiurnal (black) and diurnal (blue) bands. The red thick line represent the density difference between depths of 100 and 20 m (scale on the rhs).

$$p'(z) = \rho \left(\int_{-z}^0 N^2(z') \eta(z') dz' - \frac{1}{H} \int_{-H}^0 \int_{-z}^0 N^2(z') \eta(z') dz' dz \right) \quad (4)$$

where N is the buoyancy frequency and η is the vertical displacement of isotherms induced by internal tides. N is calculated using monthly averaged temperature and salinity data from the mooring. The vertical displacement η associated with internal tides is calculated as,

$$\eta(t, z) = \frac{T'(t, z)}{\overline{dT}/dz} \quad (5)$$

with \overline{T} representing the time-average of temperature and the fluctuating temperature is defined as

$$T'(t, z) = T(t, z) - \overline{T}(z). \quad (6)$$

The variable η is estimated using temperature data available in the 20–100 m depth range. Harmonic analysis is performed to extract η associated with the M_2 and K_1 internal tides. Subsequently, η is linearly interpolated to velocity depths. It should be noted that in the energy flux calculation using our model, density is used to estimate η instead of temperature (see Section 4.2).

The temporal evolution of currents, pressures and energy flux associated with the internal tides of M_2 and K_1 during March is shown in Figure 3. It is important to carefully interpret the energy flux based on data from a single

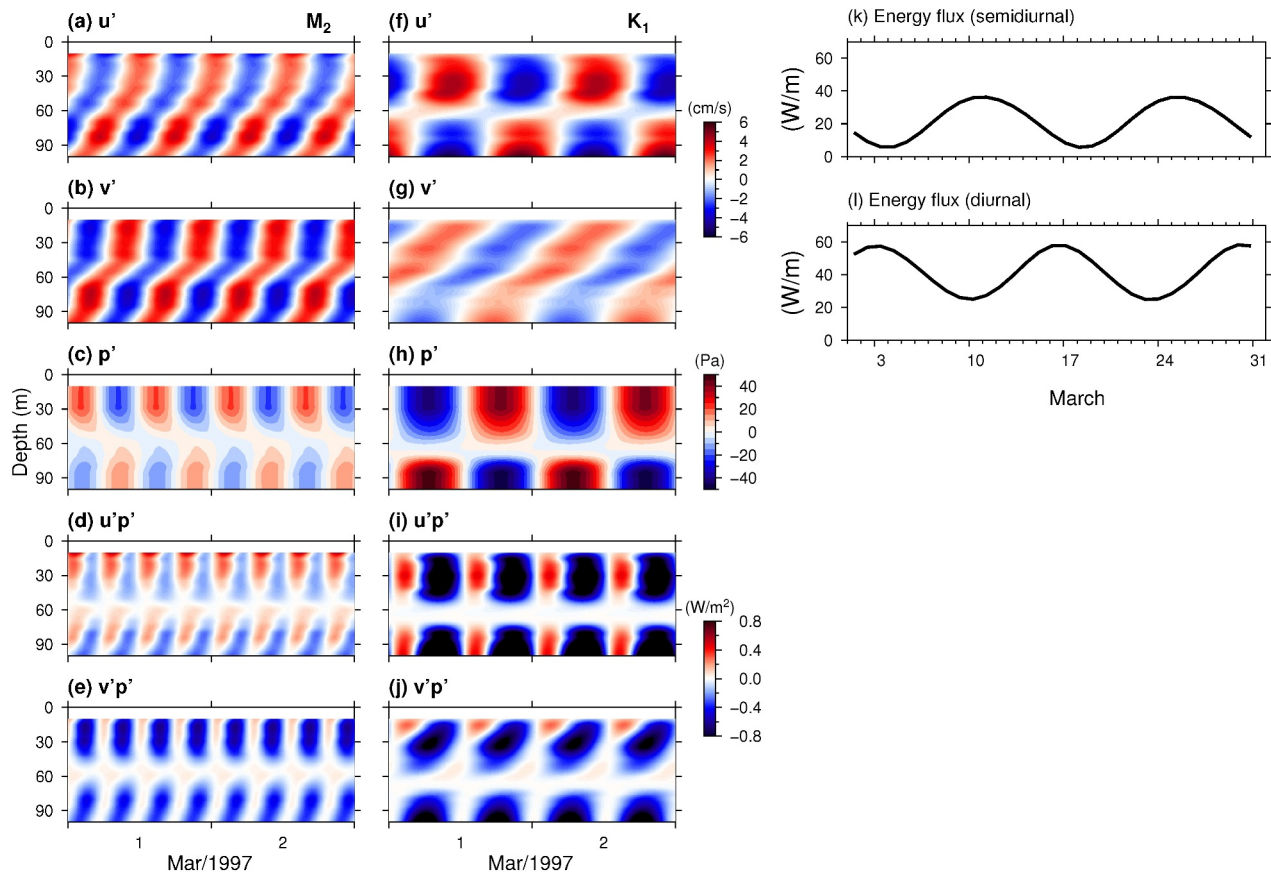


Figure 3. Depth-time series of the internal tides for the (left column) M_2 and (middle column) K_1 frequencies: (a, f) eastward velocity u' , (b, g) northward velocity v' , (c, h) baroclinic pressure p' , (d, i) eastward energy flux, and (e, j) northward energy flux during March. Color scales are on the rhs of the middle column. The right column shows the time evolution of the vertically integrated time-averaged energy flux for the (k) semidiurnal and (l) diurnal internal tides during March. Scale on the lhs.

mooring, as the results can vary significantly depending on the mooring's location relative to the generation site and the propagation characteristics of internal tides from those sites. March was selected as a representative month because the basic structure of baroclinic currents and pressure remains relatively similar throughout the year. The vertical structure of baroclinic currents and pressure exhibits dominant first-mode signals at both frequencies (Figures 3a–3j). The baroclinic pressure reaches 20 Pa for M_2 and 45 Pa for K_1 . The displacement of the sea surface associated with these values is approximately 0.2 and 0.45 cm for M_2 and K_1 respectively; sea surface elevation of the M_2 internal tide in the SH from satellite data also shows similar values (Ma et al., 2021). As with baroclinic currents, a clear spring-neap cycle is seen in the semidiurnal and diurnal baroclinic pressure (not shown). The K_1 energy flux is twice as strong as that of M_2 with a depth-integrated energy flux of about 15 W/m for M_2 and 40 W/m for K_1 . The direction of the time-mean, depth-integrated energy flux is markedly different in M_2 versus K_1 ; the M_2 energy flux propagates southward, while that of K_1 propagates mainly westward (not shown). Similarly to the time series of internal tides (Figures 2d and 2e), the energy flux (Figures 3k and 3l) also shows clear spring-neap variability in both bands. The semidiurnal energy flux reaches 40 W/m or so during the spring phase, while the diurnal energy flux reaches 60 W/m. Although the barotropic forcing is similar at both frequencies, the energy flux in the diurnal band is significantly elevated.

We also computed seasonal means of energy flux to understand the seasonal variation for both semidiurnal and diurnal internal tides. The energy flux averaged for winter for M_2 is 8 W/m versus 25 W/m for K_1 . For the spring season, the values are 12 W/m and 11 W/m, respectively, and for the summer, they are 9 W/m and 18 W/m. For fall, the values are 10 W/m and 11 W/m, respectively. It is evident that the energy flux for K_1 is significantly higher in winter. In spring, the energy fluxes are more or less similar, while in summer, the K_1 energy flux is larger than in spring. We provide a detailed analysis of the seasonal energy flux in the model section (see Section 4.2).

4. Numerical Modeling of Internal Tides in the Strait of Hormuz

We now use MITgcm simulations to help place the observed internal tide variability at the mooring location in a wider context. The model also helps us decipher the generation, propagation, dissipation, and seasonal variation of the semidiurnal and diurnal internal tides in the SH. Before going into a detailed analysis, we first evaluate the model skill against observational data.

4.1. Comparison of Model With Observations

4.1.1. Temperature, Salinity and Currents

The performance of the model in representing hydrography and circulation is evaluated in Appendix A by comparing the simulated temperature, salinity, density, and currents with the mooring observations in the SH. The fidelity of the model is quantified using skill metrics such as the correlation coefficient (R), the mean square error (RMSE), and the mean absolute error (MAE) defined by:

$$skill = 1 - \frac{\sum_1^n (x_{model} - x_{obs})^2}{\sum_1^n (x_{model} - \bar{x}_{obs}) + (x_{obs} - \bar{x}_{obs})^2} \quad (7)$$

$$R = \frac{1}{n} \frac{\sum_i^n (x_{model} - \bar{x}_{model})(x_{obs} - \bar{x}_{obs})}{\sigma_{x_{model}} \sigma_{x_{obs}}} \quad (8)$$

$$RMSE = \sqrt{\sum_1^n (x_{model} - x_{obs})^2 / n} \quad (9)$$

$$MAE = \frac{\sum_1^n |x_{model} - x_{obs}|}{n} \quad (10)$$

Skill can range from 0 to 1 where 1 represents perfect agreement. In general, the model captures the observed seasonal variations, including the magnitude and vertical structure.

Given that the observed internal tides show strong seasonal change, we inspect the hydrography and circulation of the model across the SH seasonally. The monthly averaged model output for December, March and July is shown (Figure 4) along the transect across the mooring location (Figure 1). This transect spatially and temporally aligns with the hydrographic and ADCP observations made by Johns et al. (2003), as shown in their Figure 10a and b, enabling a visual comparison between the model and observations. As noted in Johns et al. (2003), there is a high-salinity layer at depth in the water column (Figures 4a–4c), particularly in March, which is most pronounced in the southern part of the SH; the observed position, magnitude, and seasonality of this high-salinity core are faithfully reflected in the model. The temperature (Figures 4d–4f) is broadly similar throughout the water column during December, warmer near the surface, and colder below in March. The density of deep water (not shown) is higher during March because of the presence of this colder, salty water. In July, the high-salinity water at depth is not as pronounced as in December, and the upper water column is warmer due to increased heating. In summary, cross sections of temperature and salinity in the SH compare favorably with observations.

To understand the role of deep outflow on the seasonality of the density structure and stratification, monthly averaged currents are extracted along this transect. The velocity components are de-tided before averaging and rotated with respect to the channel to obtain the along-strait current speed. The along-strait current is positive in the deeper water column (outflow from the AG) and negative above 30 m (inflow to the AG) (Figures 4g–4i). The deep outflow is stronger during March compared to December and July (Figure 4m), as also noted by Johns et al. (2003). The cross section of N across the mooring (Figures 4j–4l) shows that the water column is more stratified in March than in December, especially near the bottom. In December, N is controlled by salinity, but in March both temperature and salinity are important. The strong outflow in March advects dense (cold and high-saline) waters from the Gulf through the deep channel and increases stratification in the SH. In July, stratification is strong in the upper water column mainly due to a strong vertical temperature gradient caused by summertime warming at the surface.

Finally, we use a seasonal climatology prepared from MOODS data to compare the simulated temperature and salinity over the model domain. We selected 18 boxes along the AG following Swift and Bower (2003) and

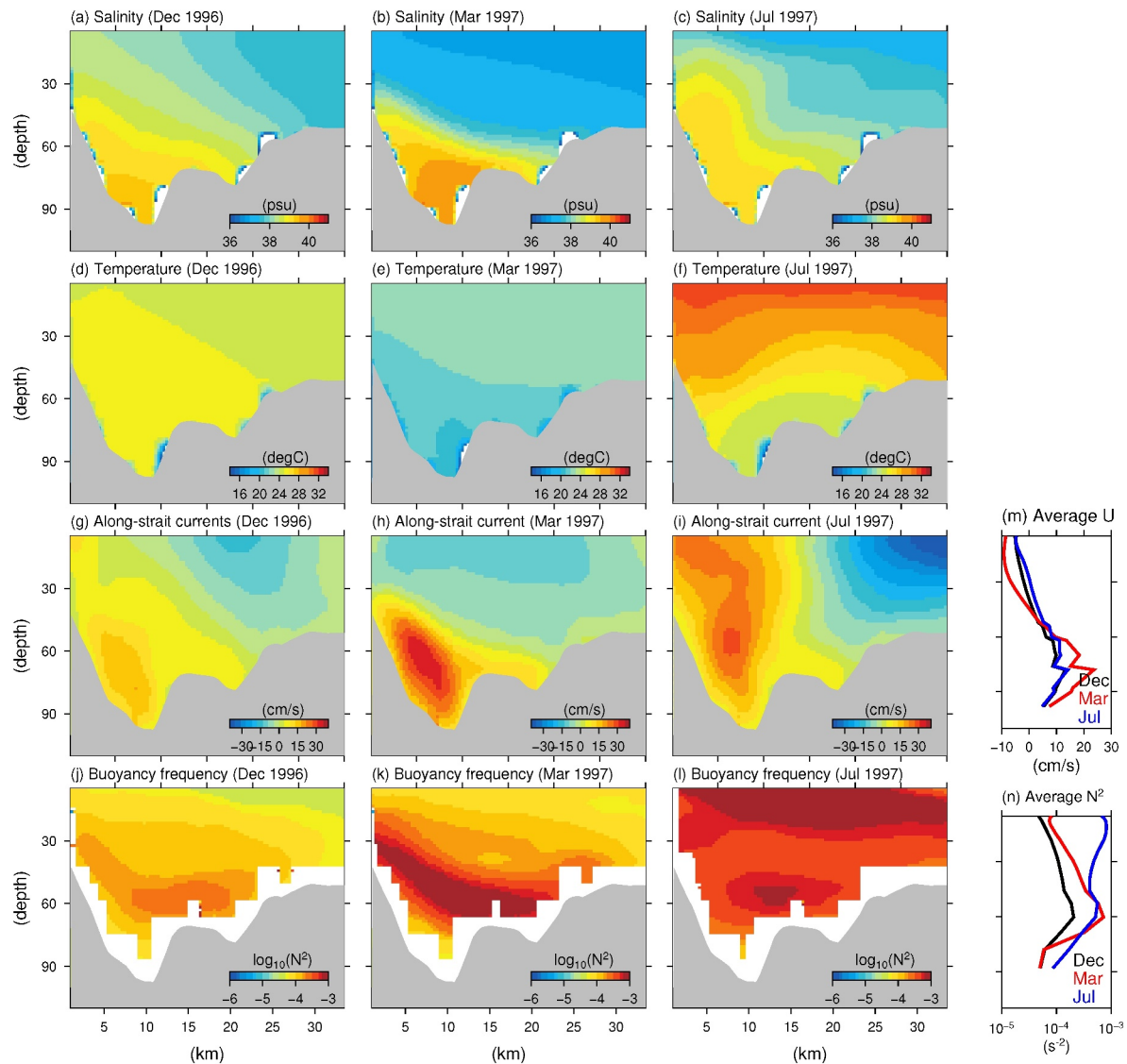


Figure 4. Monthly averaged modeled salinity (panels a, b, c), temperature (d, e, f), along-strait currents (g, h, i) and stratification N^2 (j, k, l). The lhs column is for December 1996, middle column for March 1997, and the rhs column for July 1997. Color scales are inset in the bottom right corner of each panel. (m and n) The along-strait current U — positive is directed out of the Gulf, negative inwards — and stratification N^2 , averaged along the transect in the strait shown in the upper right corner of Figure 1a, as a function of depth for December (black), March (red) and July (blue).

prepared a seasonal climatology for each box (Figures S2 and S3 in Supporting Information S1). The vertical structure of the temperature and salinity along the Gulf is then compared with the averaged model data for each box. As the aim of the comparison is to understand the capability of the model to simulate seasonal variations in hydrography, it is reasonable to compare our model year 1997 simulation with climatology data (despite the temporal mismatch between our model year and MOODS' 1940–1990 mean). Comparison of temperature and salinity for winter, spring, and summer is shown, together with skill, R, RMSE, and MAE. The model skill for temperature is 0.88 in winter and 0.96 in summer, with RMSE values of 0.86°C and 1.5°C, respectively. For salinity, the skill is 0.84 in winter and 0.82 in summer, with RMSE values of 0.5 psu and 0.63 psu, respectively. The model is able to broadly capture the observations and its clear seasonality of stratification. The winter is weakly stratified throughout the domain and the summer is strongly stratified. The high saline waters within the AG and the low salinity waters in the Sea of Oman during winter are also well represented in the model.

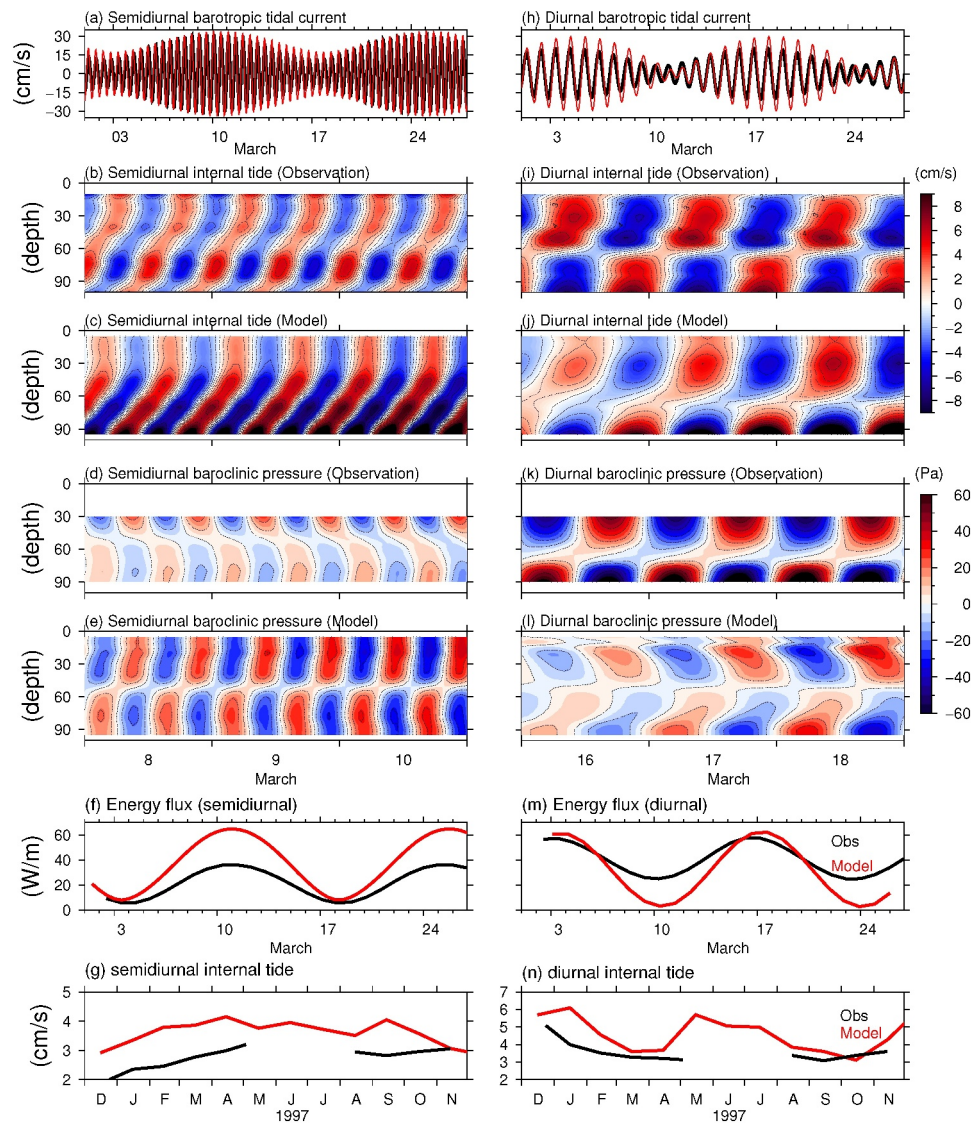


Figure 5. Comparison of simulated barotropic and baroclinic tides with observations during March. (a) Eastward component of simulated (red) and observed (black) semidiurnal barotropic tides. (b) Observed semidiurnal internal tides. (c) Simulated semidiurnal internal tides. (d) Semidiurnal baroclinic pressure (p') computed using observations. (e) Semidiurnal p' computed using model output. (f) Magnitude $\left(\sqrt{F_x^2 + F_y^2}\right)$ of semidiurnal energy flux (F) from observation (black) and model (red). (g) Vertically averaged monthly mean magnitude $\left(\sqrt{u^2 + v^2}\right)$ of semidiurnal internal tides from observation (black) and model (red). (h–n) The same (a)–(g) but for the diurnal band.

4.1.2. Barotropic and Internal Tides at the Mooring Location

Simulations of barotropic and baroclinic tidal velocities, baroclinic pressure, and energy flux for the semidiurnal and diurnal bands are compared with mooring observations in the SH (Figure 5) during March. March is selected as a representative month. Similar comparisons for other months have been conducted but are not shown. The model captures the semidiurnal and diurnal barotropic tides reasonably well (Figures 5a and 5h) with the correlation values (R) greater than 0.9 and RMSE ~ 5 cm/s. The spring-neap cycle of barotropic tides is also well captured by the model. A comparison of internal tides is shown in Figures 5b, 5c, 5i, and 5j. The phase, vertical structure, and the spring-neap variability of internal tides in both bands are reasonably well represented in the model. However, the correlation and RMSE vary with depth. The semidiurnal band has a maximum correlation (>0.9) in the upper water column (<40 m) with RMSE < 2 cm/s; in the lower water column, the value of R is in the

range of 0.5–0.8 with RMSE 2–4 cm/s. The diurnal band has a correlation of 0.5–0.9 with RMSE 2–4 cm/s at both the upper and lower depths. At the very bottom, both bands show RMSE above 5 cm/s. The simulation in both bands overestimates the observations; one possible explanation may be that the forcing due to the barotropic tides is too strong in the model. The phase of the baroclinic pressure associated with internal tides in both bands is well captured. However, the model overestimates the amplitude of the semidiurnal baroclinic pressure and underestimates the diurnal baroclinic pressure. The overestimation of currents and baroclinic pressure is reflected in the energy flux, most notably in the semidiurnal band (Figure 5f): the modeled depth-integrated energy flux is roughly 20 W/m higher than observed during spring tide. In addition to the energy flux, we compared barotropic-to-baroclinic conversion (C) (Equation 14) obtained from the mooring observations and our model. M_2 and K_1 constituents are considered as representative of the semidiurnal and diurnal band, respectively. C is found to be very small ($\sim 10^{-3}$ W/m²) for both constituents in the observations and in the model, indicating that the local generation of internal tide is negligible at the mooring location.

To assess the model's ability to capture the seasonal variation of internal tides, the monthly mean depth-averaged magnitude of internal tides in the semidiurnal and diurnal bands from both mooring observations and the model is shown in Figures 5g and 5n. In general, the model captures the observed seasonality with a positive bias. Consistent with observations, the model simulation shows strong internal tides in the diurnal band and weak internal tides in the semidiurnal band during winter. Both observations and the model indicate a gradual increase in semidiurnal internal tides from December to May, and a decrease in diurnal internal tides from December to April. It should be noted that the model predicts strong diurnal internal tides during May–July, which cannot be confirmed because of the lack of observations during this period. A detailed discussion on the seasonal variability of internal tide energetics will be provided in the next section.

In Appendix B, we assess the ability of the model to simulate the sea level associated with M_2 and K_1 tides using tide gauge observations along the coast of AG and the Sea of Oman (Figure B1). We also used mooring observations within the Gulf (Michael Reynolds, 1993) to evaluate the tidal currents associated with M_2 and K_1 (Figure B2). Both tides and tidal currents compare well for both constituents. Also note the model is able to reproduce the residual cyclonic circulation inside the Gulf (Figure B2c).

In summary, we find that the model does a good job simulating tidal flow, both at tidal frequencies and over the seasonal cycle, which justifies its use to explore the generation and propagation of internal tides in the SH.

4.2. Generation and Propagation of Internal Tides in the Strait of Hormuz

4.2.1. Energy Flux and Barotropic-To-Baroclinic Conversion

To identify the generation sites of internal tides in the SH we calculate the criticality parameter (γ) defined as the ratio of the topographic slope (ζ) to the slope of the wave characteristic (s) (Cacchione et al., 2002),

$$\gamma = \frac{\zeta}{s} = \frac{\sqrt{(\partial h/\partial x)^2 + (\partial h/\partial y)^2}}{\sqrt{(\omega^2 - f^2)/(N^2 - \omega^2)}} \quad (11)$$

where ω is the frequency of the internal tide, h is the depth of the water column, f the Coriolis parameter, and N the buoyancy frequency. The topographic slope is classified as subcritical ($\gamma < 1$), critical ($\gamma = 1$), or supercritical ($\gamma > 1$). Barotropic tidal flow across a critical or supercritical topography can efficiently transfer barotropic to baroclinic tidal energy through tide-topography interaction (Shaw et al., 2009). The criticality parameter for M_2 and K_1 , estimated using the annual mean bottom N and topographic slope of the model, is shown in Figure 6. Both critical and supercritical topography is found at both frequencies at the bathymetric highs and adjacent coastal regions, and so we can expect efficient barotropic-to-baroclinic energy transfer in these regions.

The spatial distribution of the M_2 and K_1 barotropic tidal ellipses, shown in Figure 7, can help us to understand the barotropic forcing in the SH. Rectilinear ellipses for both constituents demonstrate the unidirectional flow of the barotropic tides in the SH. The spatial distribution of the tidal ellipses implies a strong tidal forcing at both frequencies with similar magnitude and orientation. The M_2 and K_1 tidal ellipses constructed from mooring observations are shown in red; note that the magnitude and orientation of the tidal ellipses at the mooring locations are similar in both observations and the model. Strong internal tide activity is expected in both frequencies in the

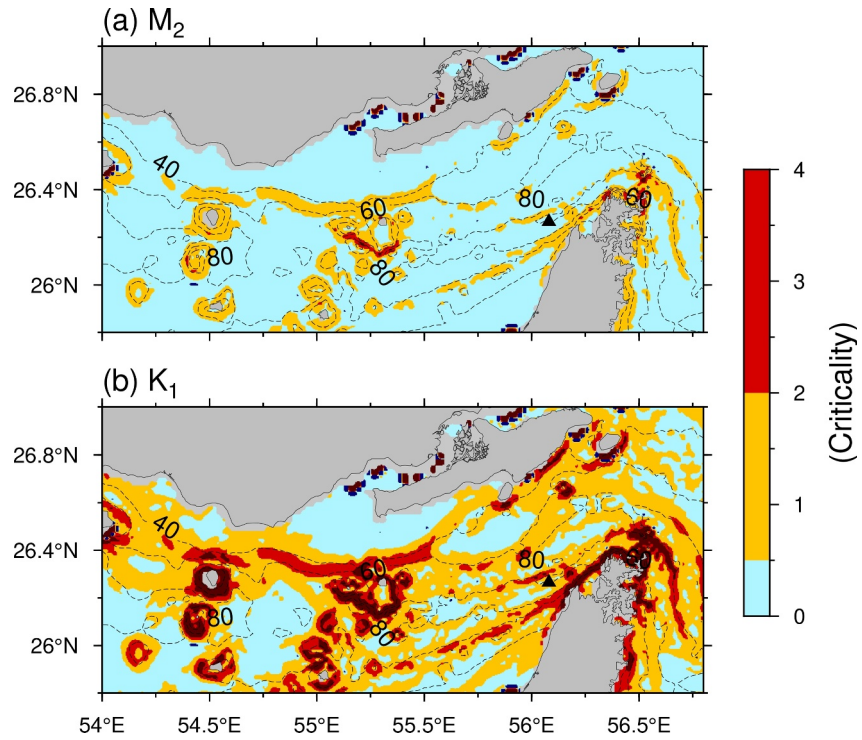


Figure 6. Criticality parameter (Equation 11) for the M_2 and K_1 frequency band calculated using yearly averaged stratification N^2 . The mooring location is denoted by the black triangle and depth contours are also marked.

SH because strong barotropic tides exist in the presence of critical and supercritical topographies. We will test this further by estimating the internal tide energy flux and conversion rate.

To determine the propagation characteristics of the semidiurnal and diurnal internal tides at the mooring location, we computed the energy flux and barotropic-to-baroclinic conversion term in the energy budget equation. The depth-integrated, time-averaged energy balance equation (Carter et al., 2008) for internal tides is given as follows:

$$\frac{\partial}{\partial t}(\overline{HKE} + \overline{APE}) + \nabla_H \cdot \overline{\mathbf{F}} = \overline{C} - \overline{D}, \quad (12)$$

where the overbar denotes integral over depth, HKE is HKE (see Equation 1), APE is the available potential energy, $\nabla_H \cdot \overline{\mathbf{F}}$ is the divergence of the baroclinic internal tide energy flux, C and D are the barotropic to baroclinic conversion rate and the dissipation term, respectively.

Upon integration over the tidal period, the above equation becomes:

$$\overline{C} - \nabla_H \cdot \overline{\mathbf{F}} = \overline{D}, \quad (13)$$

Barotropic to baroclinic conversion (C) (Buijsman et al., 2012; Kelly & Nash, 2010) in Equation 12 can be expressed as

$$C = \langle \nabla H \cdot \mathbf{u}_{bt} p'_b \rangle, \quad (14)$$

where ∇H is the topographic gradient obtained from bathymetry, \mathbf{u}_{bt} is the barotropic tidal current for each constituent and p'_b is the baroclinic pressure at the bottom.

The energy flux integrated with depth (F) (Equation 2) and the barotropic to baroclinic conversion (C) (Equation 14) of the M_2 and K_1 internal tides in the SH is shown in Figures 7c–7f. These terms were computed using a full year of model simulation. Large fluxes are seen over topographic features such as the shelf break and sills.

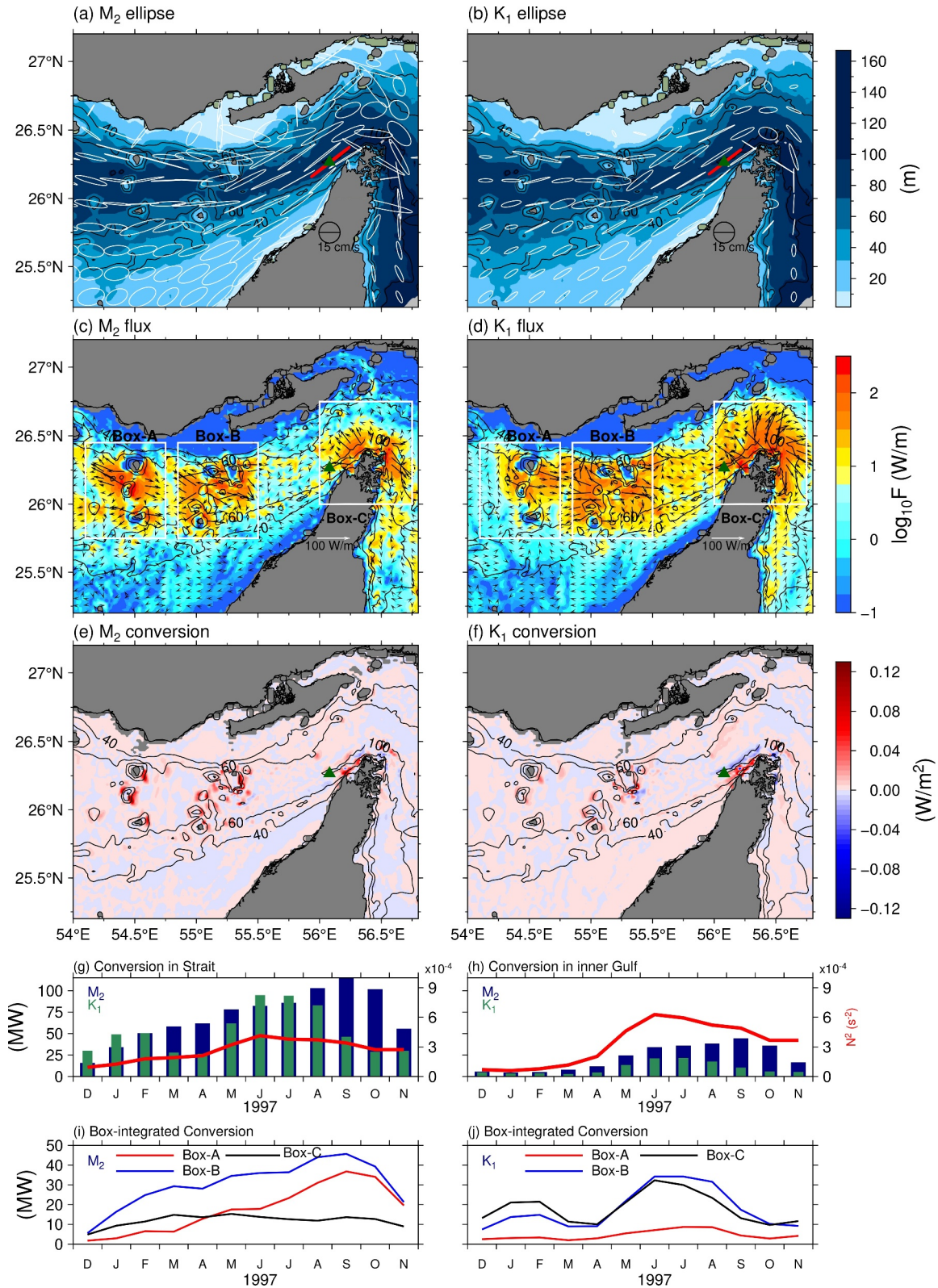


Figure 7.

The energy flux of M_2 (K_1) over the generation sites exceeds 70 W/m (150 W/m), reaching a maximum of 100 W/m (300 W/m). Differences in the direction of the energy flux vectors at the two frequencies show that the rather complex propagation characteristics of the internal M_2 and K_1 tides differ from each other, even though the generation sites are the same. The flux originates near the topographic source and propagates away, losing its energy within a few tens of kilometers.

The dominant source regions for internal tides in the SH are marked in Boxes A, B and C in Figures 7c and 7d. Box A and B are comprised of several small bathymetric highs that act as internal tide generation sources for both frequencies. The maximum conversion is ~ 0.1 W/m² at the generation sites in both bands. Efficient conversion takes place at supercritical topography: The area-integrated C in Box A and B is ~ 14 MW (4 MW) and 25 MW (17 MW) for M_2 (K_1) frequencies. Thus, in both Boxes A and B, the conversion is dominated by M_2 , with energy flux vectors oriented along the SH, roughly in the same direction as the semimajor axis of the barotropic tides (Figures 7a and 7b). The maximum conversion takes place between depths of 60–80 m. The strong barotropic tides across this topographic slope are likely the reason for locally strong internal tides. The amplitude of the tidal ellipses indicates that the barotropic forcing for M_2 is significantly stronger than K_1 across the sills in Boxes A and B; this could explain the relatively high conversion rate at this frequency. See the supplementary for a zoomed in view of the magnitude of the barotropic tidal currents M_2 and K_1 in Boxes A and B (Figure S4 in Supporting Information S1). In Box C, the internal tides are generated from steep topography near the coast and propagate toward the deepest part of the SH. Positive conversion is found over steep topography between depths of 40–80 m. The mooring site is located close to this generation site. In Box C, a negative conversion rate is observed at a depth of 100 m (Figure 7c). Although a large energy flux is found in these regions, the sign is always negative, primarily due to the out-of-phase relationship between local barotropic tides and baroclinic pressure (Carter et al., 2012). The area integrated C here is approximately 14 MW for M_2 and 17 MW for K_1 , indicating the predominance of K_1 internal tides. The barotropic forcing for the M_2 and K_1 frequencies was found to be similar in this region (Figures 7a and 7b).

Finally, we analyze the variation of the conversion around its annual mean to document the seasonal variation of internal tides in the SH. The monthly mean of C integrated over SH (54–57°E, 25.2–27.2°N) at both frequencies is shown in Figure 7g (note that only positive values of C are included in the integration). The monthly mean of C integrated over the inner Gulf (47–54°E, 22–31°N) is also shown (Figure 7h). Compared to the inner Gulf region, SH shows a strong conversion in the components M_2 and K_1 . In the inner Gulf, M_2 is the dominant internal tidal energy relative to K_1 throughout the year. C shows clear seasonality with weak conversion during the winter and spring seasons and stronger conversion during the summer and fall seasons. Note that in the SH, the band that dominates the area-integrated conversion varies over the seasonal cycle. Specifically, K_1 is higher during December–January and June–July, M_2 conversion dominates in March–May and August–November. To understand whether this variation is consistent in our three boxes, we present the integrated monthly conversion within each box for both components (Figures 7i and 7j). In boxes A and B, the conversions of K_1 and M_2 are relatively similar in December–January. However, in Box C, K_1 shows a much larger conversion compared to M_2 . In March–April, M_2 dominates K_1 in all boxes. During June–July, the strong conversion of K_1 in boxes B and C is reflected in the dominance of this frequency in the area-integrated conversion for the SH. The dominant M_2 conversion from August onward noted in the SH is due to the strong conversion at this frequency in boxes A and B.

A time series of the monthly mean vertically averaged buoyancy frequency ($N^2 = -\frac{g}{\rho_0} \frac{\partial \rho}{\partial z}$; where ρ is the density) is plotted for both the SH and the inner Gulf (Figures 7g and 7h). In the inner Gulf, weak stratification during winter probably accounts for the significantly reduced activity of the internal tide during this period. However, in the SH, the response of M_2 and K_1 internal tides to seasonal stratification differs. M_2 internal tides follow the seasonal variation of stratification, showing weak conversion in winter when stratification is weak and strong

Figure 7. (a)–(b) Barotropic M_2 and K_1 tidal ellipses in the Strait of Hormuz (SH) computed from model output. The ellipse constructed using mooring data is shown in red at the position of the green triangle. Bathymetry is shaded. (c)–(d) Annual-mean (Dec 1996–Nov 1997) of depth-integrated internal tide energy flux for M_2 and K_1 . Energy flux vectors are also shown along with their scale. (e)–(f) Annual-mean of depth-integrated barotropic-to-baroclinic energy conversion (C) (Equation 14) of the M_2 and K_1 internal tides. (g)–(h) Monthly mean of area-integrated C in the SH (54–57°E, 25.2–27.2°N) and in the inner Gulf (47–54°E, 22–31°N). Monthly mean of vertically averaged N^2 for SH and the inner Gulf is shown as a red line. (i)–(j) The area-integrated conversion for M_2 and K_1 in Box A, B, and C.

conversion in the remaining months when stratification is strong. In contrast, K_1 shows strong conversion even during the weak stratification in winter. This is particularly evident in Box C, where the mooring location is located. In the next section, we will further investigate the role of seasonally varying barotropic tides and stratification on the seasonal variation of internal tides at the generation site near the mooring location.

4.2.2. Seasonality of Internal Tides at the Mooring Location

Figures 8a and 8b show the annual mean C for the M_2 and K_1 constituents at the location of the mooring. The energy flux vectors averaged over 1 year are also plotted. The dominant source of internal tides close to the mooring location is marked as Box B, with Box A representing the mooring site (a second large generation source of internal tides is to the northeast of Box B). In Box B, values of C exceeding 0.1 W/m^2 are found along steep topography at depths between 40 and 80 m for both M_2 and K_1 . The K_1 conversion dominates that of M_2 , but the region of maximum conversion is similar in both. The energy flux vectors show that the internal tides generated here propagate to deeper parts of the SH. The negative values of C in the deeper part of this site are likely due to shoaled internal tides from these generation sites, as found in earlier studies conducted in other regions (Kang & Fringer, 2012; Zilberman et al., 2009). The yearly average energy flux in Box B is $\sim 50 \text{ W/m}$ for M_2 and $\sim 170 \text{ W/m}$ for K_1 . The same in Box A is $\sim 17 \text{ W/m}$ and $\sim 43 \text{ W/m}$ for M_2 and K_1 , respectively.

To further examine the seasonal variation of the energetics of internal tides, we plotted the conversion of M_2 and K_1 and the energy flux for December, March and August (Figures 8c–8h), representing the winter, spring and summer seasons, respectively. Recall that in December, mooring observations show weak internal tides for M_2 but strong values for K_1 , and strong internal tides for both constituents in March (Figure 2). In December (March), the box-averaged M_2 energy flux at the generation site is $\sim 14 \text{ W/m}$ ($\sim 100 \text{ W/m}$) and at mooring site it is $\sim 5 \text{ W/m}$ ($\sim 33 \text{ W/m}$). Thus, the results of the model also show that the M_2 internal tidal energy is weak in December and strong in March. In contrast, the K_1 energy is larger in December with a large flux and conversion. In December, the box-averaged K_1 energy flux at the generation site is $\sim 130 \text{ W/m}$ and at the mooring site it is $\sim 76 \text{ W/m}$. During March, the energy associated with the two constituents is of similar magnitude. The M_2 and K_1 conversions and the criticality parameters across the generation site are plotted in Figures 8i and 8j. In March, the topography at the generation site is near-critical for M_2 and supercritical for the K_1 internal tide; conversion of the M_2 internal tide is slightly higher than that of K_1 , indicating that stratification (Figure 4k) favors the generation of the M_2 internal tide. The area integrated C for SH (Figure 7i) also indicates a greater conversion for M_2 than for K_1 during March, suggesting that stratification in the strait is more favorable for the generation of M_2 internal tides. In December, the generation site is subcritical (Figure 8i) for the M_2 internal tides due to weak stratification (Figures 4j and 8k) while it is supercritical for K_1 (see also Figure S5 in Supporting Information S1). This leads to a weak C for M_2 and a strong conversion for K_1 . The area integrated C for SH (Figure 7g) shows a larger conversion for K_1 during December, suggesting that in this month the stratification in SH is more favorable to K_1 internal tide generation than that of M_2 . In August, the M_2 conversion is similar to that in March, with K_1 also showing strong conversion.

The monthly mean of spatially integrated conversion for Box B over the year for both M_2 and K_1 is presented in Figures 8k and 8l. Furthermore, we show the box-averaged vertical-mean of N^2 and the bottom criticality parameter. For the M_2 frequency, the topography is subcritical from December to January and critical for the remaining months. The area-integrated conversion (C) reflects this pattern, with a minimum conversion in winter and a stronger conversion during the other months. For K_1 , the topography remains supercritical throughout the year, facilitating efficient energy transfer. However, the K_1 conversion is relatively weak during March–May and September–November, despite the supercritical topography, and reaches its maximum from June–August.

Next, we analyze the seasonal variation of barotropic tidal currents at the generation site. The spatially averaged monthly mean magnitude ($\sqrt{u_{bt}^2 + v_{bt}^2}$) of the barotropic tidal currents for M_2 and K_1 is shown in Figures 8k and 8l. The M_2 barotropic tidal current exhibits negligible variation throughout the year. In contrast, K_1 shows significant seasonal variation, with two distinct peaks occurring in winter and summer, similar to the seasonal variability of internal tides.

In a recent study, Tanaka (2024) showed that the vertical structure of coastally trapped superinertial ($\omega/f > 1$; where ω is the tidal frequency and f is the Coriolis frequency) internal tides can become more barotropic on shallow slopes. As our study region lies between 20°N and 30°N , where ω/f ranges from 1 to 1.5 for diurnal frequencies, there is potential for the trapping of superinertial internal tides at this frequency with barotropic

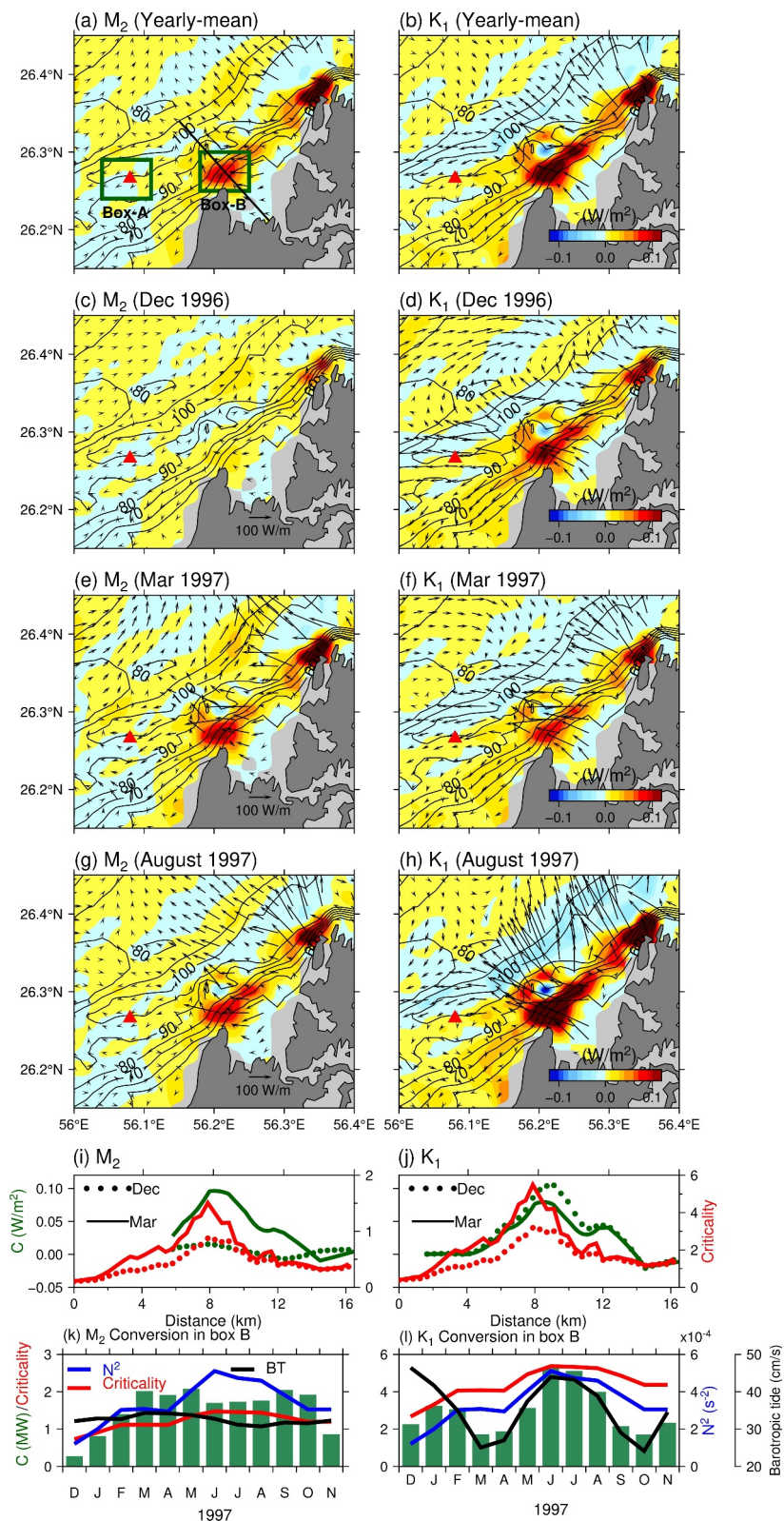


Figure 8.

vertical structure along the coast. It is thus important to understand whether the observed variation in magnitude of diurnal barotropic tides is caused by coastally trapped internal tides.

To investigate this, we computed the modal structure of the trapped diurnal internal tides across the generation site (black transect in Figure 8a) by solving the eigenvalue problem in a two-dimensional plane (y – z) using the equations detailed in Tanaka (2024). Refer to Appendix C for detailed information on the model configurations and experiments. Our findings indicate that trapped diurnal internal tides are less developed in the superinertial case than in the subinertial case in the study region, with a more pronounced baroclinic vertical structure (Figure C1). Thus, the intensification of barotropic tides at the generation site due to trapped waves can be ruled out. However, the diurnal internal tides that propagate along the coast likely influenced by these trapped waves remain beyond the scope of this study.

Finally, our model simulations reveal that the seasonal variation in K_1 barotropic tides extends beyond the internal tide generation site and its vicinity, encompassing the entire Gulf. The magnitude of K_1 barotropic tidal currents at various locations within the model domain is presented in the supplementary material (Figure S6 in Supporting Information S1), which demonstrates seasonal patterns consistent with those observed at the mooring location and generation sites. M_2 shows negligible seasonal variation in the Gulf. Non-astronomical changes in K_1 barotropic tidal forcing may play a critical role in the seasonality of diurnal internal tides in the region. The seasonal variation in conversion largely follows the seasonal variation of barotropic tidal forcing at the generation site near the mooring location (Figure 8l). In winter, the combination of supercritical topography and strong barotropic tides intensifies diurnal internal tides. In spring, despite supercritical topography, weak barotropic forcing results in weak internal tides. In summer, strong stratification and barotropic forcing lead to efficient internal tide generation. In fall, relatively weak stratification combined with weak barotropic forcing results in weaker internal tides at K_1 frequency.

Finally, we examine the seasonal variation of internal tide dissipation at the mooring location. Local dissipation of internal tides (Egbert & Ray, 2001; Niwa & Hibiya, 2004) is estimated as the difference between the local conversion and the radiation,

$$D = C - \nabla \cdot F. \quad (15)$$

The dissipation derived from the model may also include other budget terms, such as advection, tendency, and numerical dissipation. Hence, while we describe D as dissipation, it is calculated as a residual of the other terms and may be negative in certain locations or times. Despite this, this approach is commonly used to estimate baroclinic energy dissipation (Jithin et al., 2020; Subeesh et al., 2021). Alford et al. (2011) observed that the spatial distribution of observed dissipation is aligned with those estimated from model simulations using Equation 15.

The spatial distribution of the internal tide dissipation integrated in depth for both M_2 and K_1 during December, March, and August is shown in Figure 9. The dissipation of the M_2 internal tide is weak during December and strong in March and August (Figures 9c, 9e, 9g, and 9i). K_1 dissipation is strong in all 3 months, with the maximum dissipation in August (Figures 9d, 9f, 9h, and 9j). The monthly mean of spatially integrated dissipation for Box B throughout the year for both M_2 and K_1 is presented in Figures 9k and 9l, along with the conversion term. The seasonal variation in the dissipation rate is consistent with the conversion. The difference between conversion and dissipation indicates that, for M_2 , a significant portion of the internal tides dissipates locally and thus is readily available for vertical mixing. For K_1 , although local dissipation is strong, a significant portion of the internal tides radiate away from the generation site and dissipate remotely. The near-critical topography

Figure 8. Barotropic-to-baroclinic conversion (C)—defined in Equation 14—of the M_2 and K_1 internal tides computed from the model simulations. Depth-integrated energy flux (F) vectors are overlaid. (a)–(b) C and F for the annual mean period (Dec 1996–Nov 1997). (c)–(h) C and F for December 1996, March 1997 and August 1997. C is shaded in color and the scale of the vector F is given. The mooring location is denoted by the red triangle. The black contours show the bathymetry. (i)–(j) The conversion C (green line) and the criticality parameter (red line) for M_2 and K_1 is plotted along the transect shown by the black line in panel (a). Continuous lines are for March and dotted lines are for December. Scales for conversion (criticality) are on the left (right) respectively. (k–l) Monthly mean of area-integrated C for M_2 and K_1 over the year for Box B. The red line indicates the box-averaged criticality, with the scale for conversion and criticality on the left. Additionally, the blue line represents the monthly mean of vertically averaged N^2 for Box B, with the scale on the right axis. The black line shows the magnitude $\left(\sqrt{u_{bt}^2 + v_{bt}^2}\right)$ of barotropic tidal currents (cm/s) averaged over Box B for M_2 and K_1 , with the scale on the rightmost axis.

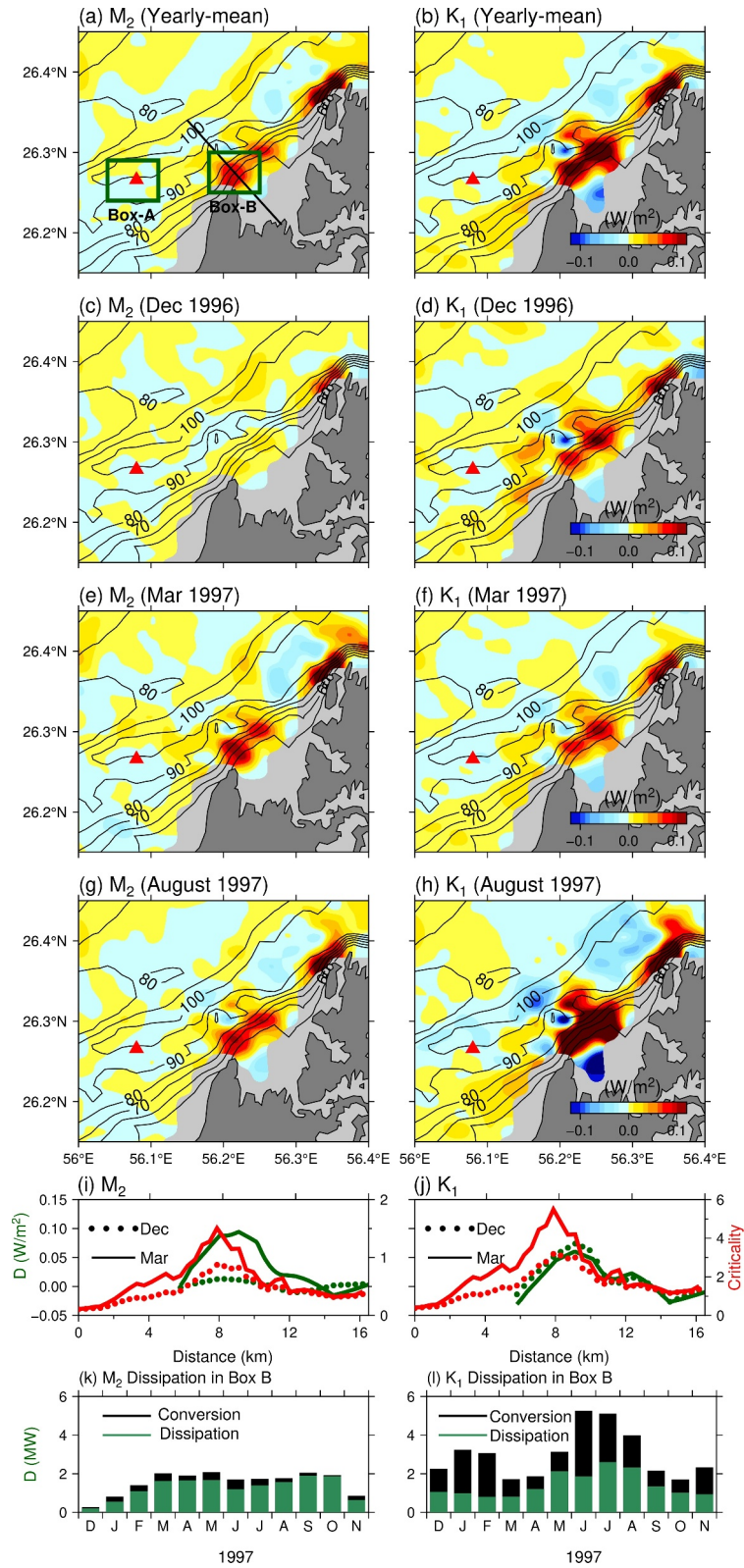


Figure 9.

probably contributes to the high percentage of local dissipation for M_2 frequency. However, for K_1 , the supercritical topography allows the waves to radiate away more effectively (Figures 9i and 9j). The effective eddy diffusivity obtained from the model (not shown) indicates elevated mixing throughout the water column at the generation sites. The magnitude of the resultant eddy diffusivity indicates that the internal tide-induced mixing is significant in the SH. However, because of the lack of direct observations of vertical mixing in the SH, this cannot be independently verified.

5. Discussion and Conclusion

The seasonally varying generation, propagation, and dissipation of internal tides in the SH has been explored using observations and a high-resolution numerical model. Mooring observations show significant low-mode internal tides in both the semidiurnal and diurnal tidal bands, but with the diurnal component dominating for most of the period. The energy flux estimated from observations shows that the semidiurnal energy flux reaches 40 W/m and the diurnal energy flux reaches 60 W/m during the spring tide. These values are moderate compared to typical energy flux levels on shallow continental shelves (e.g., 80 W/m on the Washington shelf (Alford et al., 2012); 130 W/m in the New England Shelf (MacKinnon & Gregg, 2003); 50–300 W/m on the shelf off the west coast of India (Subeesh et al., 2021)), but small compared to continental slopes and deep ocean (Jithin et al., 2020; Subeesh et al., 2021).

Our model simulations show that there are multiple internal tide generation sites in the SH. Rich topographic features such as bathymetric highs and steep topography near the coast act as internal tide generation sources for both semidiurnal and diurnal internal tides. The low-mode internal tides generated by these topographic features lose their energy within a short distance. The conversion and dissipation diagnostics of the energy budget equation suggest that most of the energy which is converted at topographic features dissipates locally. However, the mechanism for this dissipation needs to be further studied.

The main focus of our study has been to understand the mechanism behind the seasonal variations of observed semidiurnal and diurnal internal tides. Our study shows that strong stratification in the spring to fall seasons supports both semidiurnal and diurnal internal tides. However, observations show that the K_1 internal tides are surprisingly large during winter when the stratification is weak. As the criticality parameter depends on the stratification of the water column, the generation of internal tides can be strongly modulated by changes in stratification. Theory suggests that internal tides of different frequencies may respond differently to this stratification. For example, Kawamura et al. (2006) noted the occasional intensification of the semidiurnal internal tide energy near the bottom of Bungo Channel, Japan, when the bottom slope of the channel becomes nearly critical to the semidiurnal internal tides. Duda and Rainville (2008) reported an increase in diurnal internal tides relative to the semidiurnal frequency when the topography becomes near-critical to the diurnal frequency. Many studies have reported the amplification of internal tides of semidiurnal and diurnal frequencies on shallow continental shelves, shelf breaks, and continental slopes when topography is near-critical with respect to frequencies (Jithin et al., 2017; Subeesh & Unnikrishnan, 2016). Estimates of the criticality parameter from our simulation show that during winter the topographic features in the SH become subcritical to M_2 internal tides and supercritical to diurnal internal tides, thus making the topography favorable for the generation of K_1 internal tides.

Enhanced barotropic tidal forcing at diurnal frequency is observed during both winter and summer in observations and model results. Seasonal variations in barotropic tides have also been documented in other ocean regions, particularly in shallow seas (Devlin et al., 2017; Haigh et al., 2020; Müller, 2012; Yan et al., 2020). These variations can be attributed to several factors, including large-scale circulation, ocean stratification, sea level changes, and surface winds (Haigh et al., 2020). During winter, the combination of strong barotropic tidal forcing and supercritical topography intensifies diurnal internal tides. The model further suggests that the maximum barotropic-to-baroclinic energy conversion for diurnal frequencies occurs in summer, driven by strong stratification and enhanced barotropic tides. However, due to a lack of velocity observations for most of

Figure 9. Depth-integrated dissipation rate (D) (Equation 15) of the M_2 and K_1 internal tides computed from the model simulations for (a)–(b) yearly averaged period, (c)–(d) December, (e)–(f) March, and (g)–(h) August. D is shaded in color along with its scale. The mooring location is denoted by the red triangle. The black contours show the bathymetry in m . (i)–(j) The dissipation D (green line) and the criticality parameter (red line) for M_2 and K_1 is plotted along the transect shown by the black line in panel (a). Continuous lines are for March and dotted lines are for December. Scales for dissipation (criticality) are on the left (right) respectively. (k)–(l) Monthly mean of area-integrated C (black) and D (green) for M_2 and K_1 over the year for Box B.

the summer months, this finding cannot be confirmed. Our model results show that seasonal variation in the diurnal barotropic tide is not confined to the internal tide generation region but extends across the entire basin. Understanding the mechanisms driving the seasonal variations of diurnal barotropic tides and their influence on the seasonal variation of internal tides across the entire basin is thus crucial and needs to be studied.

The stratification in the SH is strongly affected by the deep outflow. Our model simulations illustrate that stratification, modified by deep outflow through the central Hormuz channel, has a significant impact on internal tide generation. Stratification changes modulate the criticality parameter close to topographic features in the SH. Low-frequency background circulation can have a significant influence on internal tidal variability by changing the stratification of the water column (Kawamura et al., 2006; Xu et al., 2021), and by the refraction and scattering of internal tides (Nash et al., 2012). In this study, we show that the seasonal variability of semidiurnal and diurnal internal tides in the SH is due to the change in stratification modulated by the low-frequency current.

The estimated elevation of the dissipation of the internal tides from the model simulations suggests that the vertical mixing induced by the internal tides may be significant in the SH and may play an important role in the transformation of the water mass. Thus, incorporation of tidal forcing in numerical models is important in order to faithfully represent the large-scale hydrography and circulation of the Gulf. Our recent study (Salim et al., 2024) shows that the mixing of tidal flows significantly affects the large-scale circulation in the Gulf and the transport of volume through the SH. This study points to a need for mixing measurements, combined with numerical model studies in the region, to better understand the contribution of internal tide energy to vertical mixing and water mass transformation. This remains a key objective for future research.

Finally, our model simulations show that small bathymetric highs in the strait are sources of internal tides at both semidiurnal and diurnal frequencies. The internal tides generated by these highs dissipate in a few kilometers. Most studies around the world have focused on internal tides generated by large seamounts and midoceanic ridges in the deep ocean, which propagate thousands of kilometers and dissipate remotely. Here, however, we show that small bathymetric features in shallow regions such as the straits may play a significant role in vertical mixing of nearby regions by acting as a source for small-scale internal tides. Understanding the mechanism of dissipation of internal tides in these regions and the route to mixing is therefore important and needs to be studied in detail.

Appendix A: Model Representation of Hydrography and Circulation

The simulated temperature, salinity, density and currents are compared to mooring observations in the SH (Figure 1a) to assess the ability of the model to represent hydrography and circulation (Figure A1). The velocity is de-tided, that is, the tidal signal is removed, and then averaged over one-day intervals. In general, the model broadly captures the magnitude and vertical structure of the observed seasonal variations. More specifically, in winter and spring the temperature never exceeds 25°C and shows little variation with depth in both observation and model. In contrast, salinity increases with depth throughout the year with a wintertime maximum of 40 psu at the bottom, again in both observations and model. In summer, the temperature exceeds 31°C in the upper water column. The water column is strongly stratified in spring and summer compared to winter. The major current system in the SH—surface inflow and deep outflow—is also well captured by the model, but current strengths are overestimated.

The model data at the mooring location are first interpolated to observation depths and then the statistical parameters are estimated from depth-time series data. We find the model skill for temperature and salinity to be 0.95 and 0.86 respectively. The correlation of the model temperature (salinity) with the observations is ~0.9 (0.86) with RMSE of 1.2°C (0.54 psu). The model is somewhat warmer and fresher than the observations. However, the representation of currents in the SH is less successful, with the correlation falling to 0.42 with a RMSE ~7 cm/s. High variability currents, owing to complex bathymetry, may be one of the reasons for the larger disparity. We did not attempt to tune the model, as it captures the vertical structure and temporal variability of currents sufficiently well for our purposes.

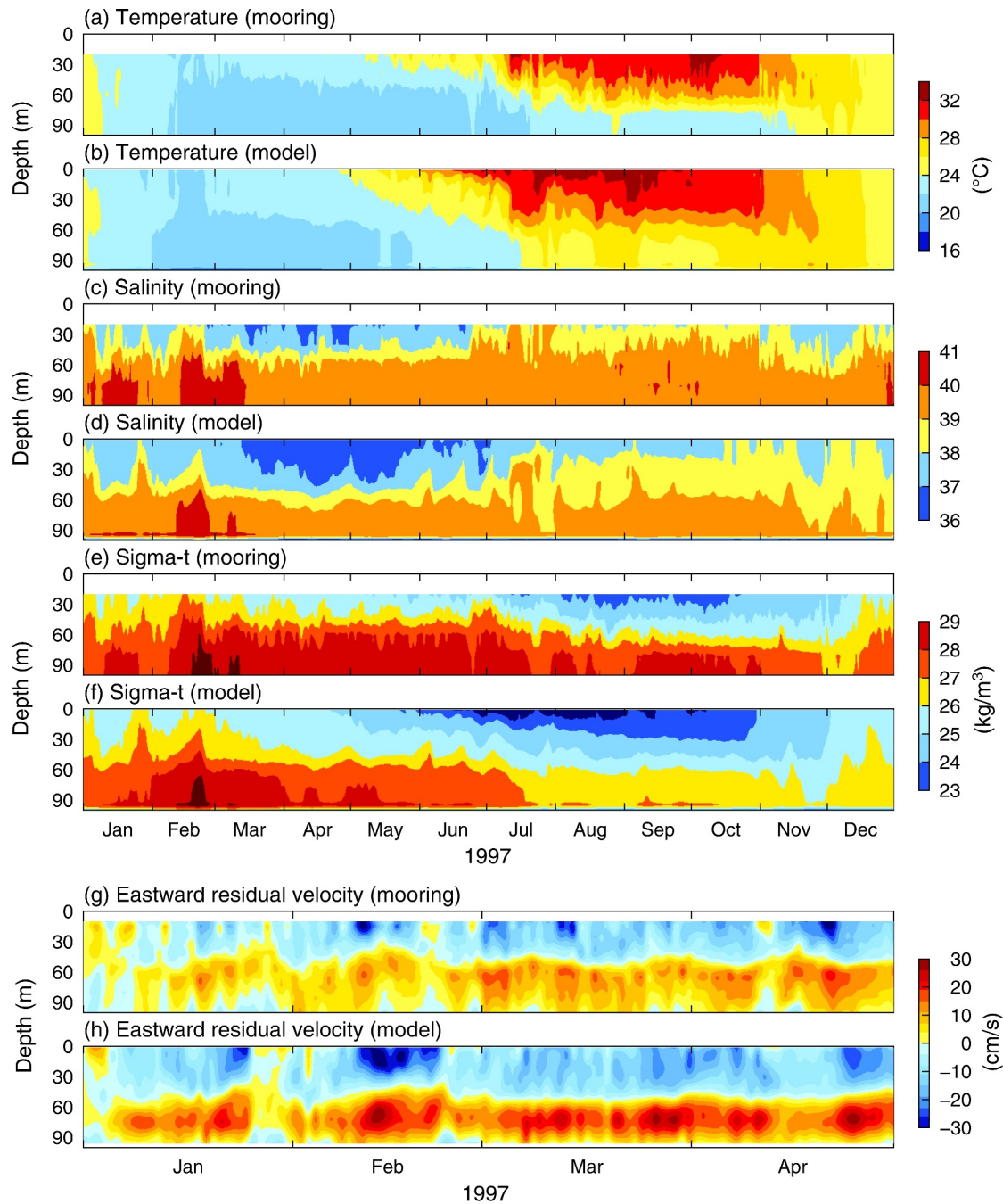


Figure A1. Comparison of model temperature, salinity, density and eastward currents (depth-time panels b, d, f, h) with mooring observations at the strait (a, c, e, g) during 1996–1997. Note that the currents are only compared for the shorter four month period, January–April 1997. The color scales are on the rhs of each pair of model-observation panels.

Appendix B: Model Representation of Tides and Tidal Currents

To evaluate the performance of the model to simulate the sea level associated with the M_2 and K_1 tides, we used the amplitude and phase of two constituents published by Pous et al. (2012), which were extracted from observations of the tide gauge along the coast of AG and the Oman Sea (Figure 1). The one-year-long sea level output from the model is extracted using the closest model grid point to tide gauge locations, and a harmonic analysis is performed to extract the amplitude and phase of the above constituents (Figure B1). Both modeled

Table A1
Names and Locations of the Moorings Used in the Arabian Gulf

Mooring Name	Longitude (°E)	Latitude (°N)	Instrument	Instrument Depth (m)	Water Depth (m)	Period	Frequency (minute)
MS	56.087	26.268	ADCP	10–85	110	15/12/1996 to 03/12/1997	30
MS	56.087	26.268	Current Meter	100	110	14/12/1996 to 16/01/1998	30
MS	56.087	26.268	Seacat	20,40,60,80,100	110	15/12/1996 to 16/03/1998	30
MS	56.087	26.268	TSKA	30,50,70,90	110	15/12/1996 to 16/03/1998	30
MB2	53.764	26.372	Current Meter	10, 30, 84	94	04/03/1992 to 29/05/1992	30
MB3	52.379	27.063	Current Meter	10, 24	81	04/03/1992 to 29/05/1992	30
MB4	51.976	26.840	Current Meter	15, 59	69	05/03/1992 to 28/05/1992	30
MB5	52.002	25.994	Current Meter	21	33	05/03/1992 to 29/05/1992	30
MB7	51.324	27.184	Current Meter	56	76	06/03/1992 to 28/05/1992	30

Note. MS denotes the mooring at the Strait of Hormuz which is represented by red star in Figure 1. Mooring names which begin with MB are from the *Mt Mitchell* expedition described by Michael Reynolds (1993) and marked in Figure 1.

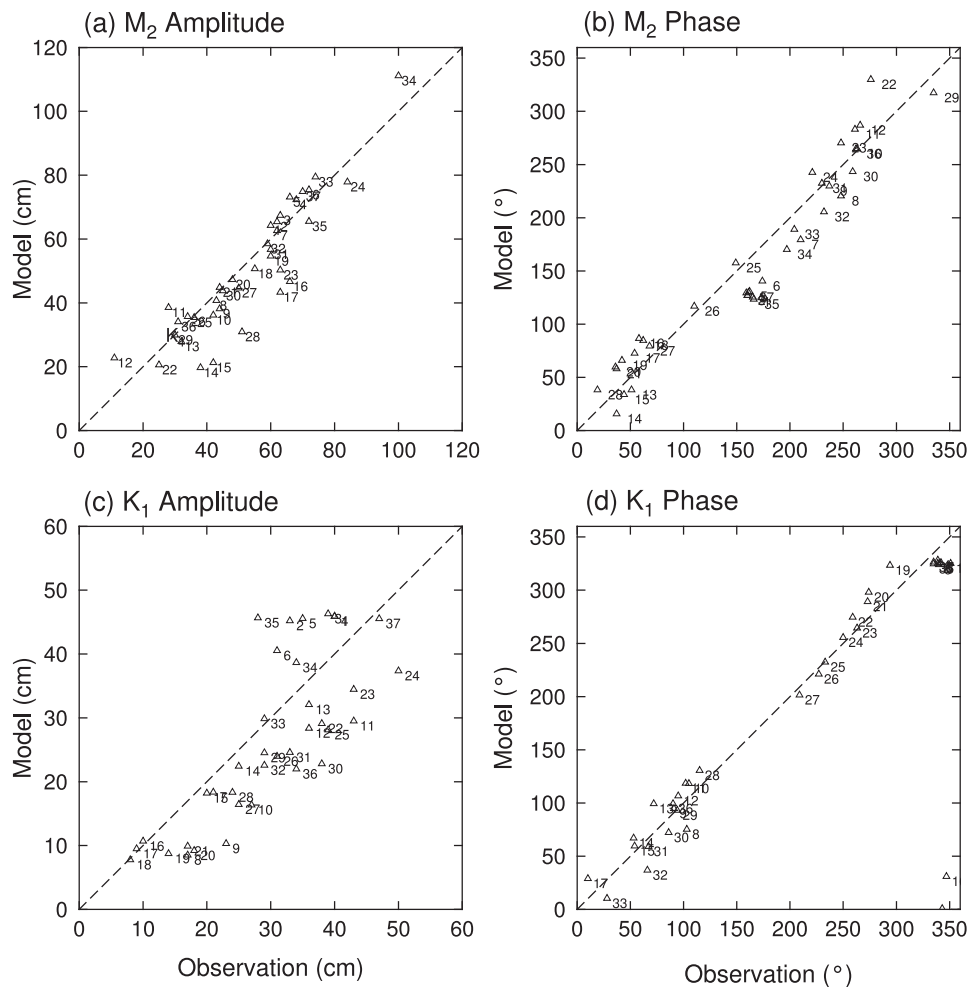


Figure B1. Comparison of the simulated elevation and phase of the M_2 and K_1 tide with tide gauge observations, the location of which is shown in Figure 1.

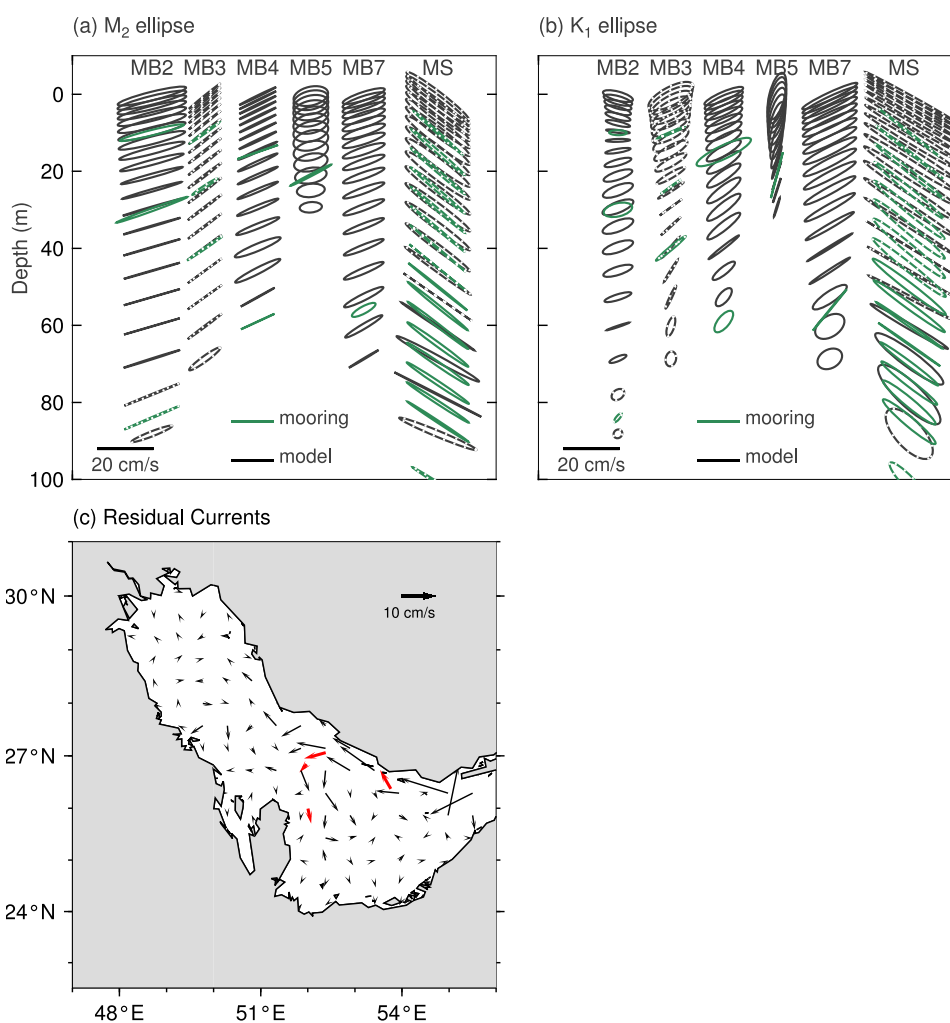


Figure B2. Comparison of simulated tidal currents and residual currents with observations in the inner Gulf and the strait. The tidal ellipse of (a) M_2 and (b) K_1 components computed from model output are plotted (in black) along with Michael Reynolds, 1993 current meter observations (in green). The bold line represents clockwise rotation and the dashed line anticlockwise rotation of tidal currents. The scale of the ellipse is marked in the lower left corner of each panel. (c) The temporal mean currents for the upper water column (0–20 m average) from March to May, derived from model simulations, are shown as black vectors. The current vectors from the uppermost current meter sensors, averaged over the same period, are depicted in red. Refer to Table A1 for the sensor positions. The scale of the vector is given in the upper right of corner of the panel.

amplitude and phase compare relatively well with observations for both constituents. The M_2 component is better captured than K_1 . We further explored the spatial pattern of M_2 and K_1 tides (not shown) and found it similar to that of earlier results such as Pous et al. (2012), Madah and Gharbi (2022), and Poul et al. (2016).

We used mooring observations inside the AG from Michael Reynolds (1993) to assess the ability of the model to simulate currents associated with the M_2 and K_1 tide. As these observations have insufficient depth coverage (see Table A1), we used total tidal currents for the comparison. Note that we compared tidal currents from 1997 simulations with observations from 1992. However, this will only mildly affect the comparison, as the amplitude and phase of a particular constituent do not vary much year to year. Our goal is to assess the capability of the model to simulate the general characteristics of tidal currents such as amplitude, propagation direction and sense of rotation of tidal currents in the inner Gulf. We conducted a harmonic analysis of the eastward and northward components of the mooring data and extracted the amplitude and phase of the M_2 and K_1 frequencies. The tidal ellipses of both constituents of the observations and the model are plotted (Figure B2). The tidal ellipses from the SH mooring are also shown for comparison. Model-simulated tidal

currents compare reasonably well with observations: They faithfully represented the amplitude, the direction of maximum current, and the sense of rotation at most of the depths. However, in MB5, the model shows a mismatch with observations, which may suggest an inability of the model to capture tides at shallow depths. It is notable that the sense of rotation of tides at most locations and depths is well captured by the model (e.g., the anticlockwise rotation of tides at the MB3 location). The variation in the sense of rotation at depth at the SH mooring location is also well captured.

Residual currents from the uppermost sensors of the current meters (Table A1) are used to validate the mean circulation inside the Gulf. Since the current meter data are only available for March–May, the comparison is conducted for this period. First, the tidal component is removed from the observations using harmonic analysis to extract the residual current. Then a temporal mean is calculated. The model currents are vertically averaged for the upper 20 m, and a map of the temporally averaged current vectors along with the current vectors from observation is shown in Figure B2. The residual circulation of the model matches well with the observations, effectively capturing the broad cyclonic circulation.

Appendix C: Modal Structure of Superinertial Diurnal Internal Tides

We computed the modal structure of the trapped diurnal internal tides across the generation site (black transect in Figure 8a). The modal structure was derived by solving the eigenvalue problem in a two-dimensional plane (y – z) using the equations detailed in Tanaka (2024). The topography was obtained using the bathymetry of the MITgcm model with the best fit across this transect. Equations were solved in a terrain-following sigma coordinates with 12 vertical and 40 horizontal grid points, maintaining a horizontal grid resolution of 750 m. Vertically averaged stratification for December is used to compute the modal structure. We conducted various

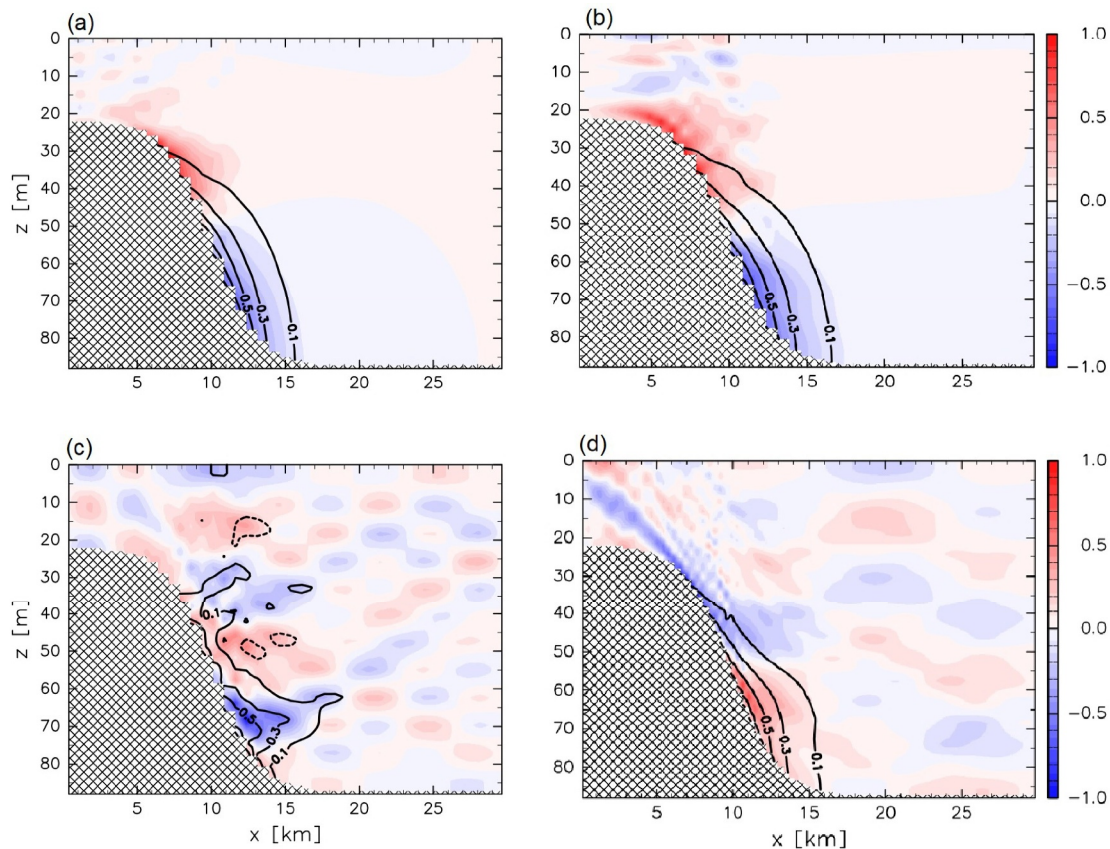


Figure C1. The modal structure of (a) subinertial ($\omega/f = 0.91$) (b) inertial ($\omega/f = 1$) (c) superinertial ($\omega/f = 1.3$) diurnal internal tides propagating along the coast. The cross-sectional structure of the pressure perturbation is shown with contours, while the along-shore velocity is shaded, with positive values indicating flow directed outward from the page. Baroclinic pressure and along-shore velocity are normalized. (d) Same as (c) but with increased horizontal resolution of 375 m.

experiments to analyze the dynamics of trapped diurnal internal tides by varying Coriolis frequencies, examining subinertial ($\omega/f = 0.9$), inertial ($\omega/f = 1$), and superinertial ($\omega/f = 1.3$) cases by fixing the topography and stratification.

In subinertial and inertial cases, distinct trapped waves were observed over the slope (see Figures C1a and C1b). However, in the superinertial case, the trapping was incomplete (Figure C1c). Increasing the horizontal resolution to 375 m enhanced the trapping to some extent (Figure C1d). It should be noted that the vertical structure of the trapped waves exhibits a baroclinic pattern near the coast, which differs from the findings of Tanaka (2024). This difference probably arises from differences in bottom topography and stratification; in our case, shallow water depth, narrow slope, and strong stratification create conditions significantly different from those of Tanaka (2024). However, more studies are needed to determine which parameter leads to this change.

Data Availability Statement

The model setup (MIT-gcm) with compile time and run time parameters can be found at http://wwwcvs.mitgcm.org/viewvc/MITgcm/MITgcm_contrib/lc_hires/lc_4320/. The Master Oceanographic Observations Dataset (MOODS), utilized in this study, originates from Alessi et al. (1999). Tidal amplitude and phase data, derived from tide gauge observations, were obtained from Pous et al. (2012), the original source being the International Hydrographic Office. Current data from mooring stations are publicly available at NOAA National Oceanographic Data Center <https://www.nodc.noaa.gov/archive/arc0001/9600082/1.2/data/>.

Acknowledgments

The authors thank the three anonymous reviewers for their constructive feedback, which helped to improve this work. The authors are grateful to Khalifa University for financial support (Grant: FSU-2020-017). The authors acknowledge support from the Federal Authority for Nuclear Regulation Project “Modeling of Radionuclide Dispersion in the UAE Environment.” JM acknowledges support from the NASA Physical Oceanography Program of the US. H. Song thanks the National Research Foundation of Korea (NRF) grant (NRF-2022R1A2C1009792) and the Korea Meteorological Administration Research and Development Program under Grant (RS-2023-00241809). The authors are very grateful to Prof. John William for providing mooring data. Dr. John K. Hall is gratefully acknowledged for providing digitalized soundings charts. The authors thank Dr. M. Salim and Alfiya Fathima for useful discussions on the MITgcm model configuration. The authors also thank Dr. Yuki Tanaka for sharing the code to compute the modal structure of coastally trapped internal tides. The numerical simulations using the MITgcm model were carried out using the Khalifa University High-Performance Computer shared facility. All plots in the manuscript were made using the open source Generic Mapping Tool.

References

- Al-Ansari, E. M. A. S., Husrevoglu, Y. S., Yigiterhan, O., Youssef, N., Al-Maslami, I. A., Abdel-Moati, M. A., et al. (2022). Seasonal variability of hydrography off the east coast of Qatar, central Arabian Gulf. *Arabian Journal of Geosciences*, *15*(22), 1659. <https://doi.org/10.1007/s12517-022-10927-4>
- Al Azhar, M., Temimi, M., Zhao, J., & Ghedira, H. (2016). Modeling of circulation in the Arabian Gulf and the Sea of Oman: Skill assessment and seasonal thermohaline structure. *Journal of Geophysical Research: Oceans*, *121*(3), 1700–1720. <https://doi.org/10.1002/2015JC011038>
- Alessi, C. A., Hunt, H. D., & Bower, A. S. (1999). *Hydrographic data from the US naval oceanographic office: Persian gulf, southern red sea, and Arabian sea 1923-1996* (Tech. Rep.). WOODS HOLE OCEANOGRAPHIC INSTITUTION.
- Alford, M. H., MacKinnon, J. A., Nash, J. D., Simmons, H., Pickering, A., Klymak, J. M., et al. (2011). Energy flux and dissipation in Luzon strait: Two tales of two ridges. *Journal of Physical Oceanography*, *41*(11), 2211–2222. <https://doi.org/10.1175/jpo-d-11-073.1>
- Alford, M. H., Mickett, J., Zhang, S., MacCready, P., Zhao, Z., & Newton, J. (2012). Internal waves on the Washington continental shelf. *Oceanography*, *25*(2), 66–79. <https://doi.org/10.5670/oceanog.2012.43>
- Alford, M. H., & Zhao, Z. (2007). Global patterns of low-mode internal-wave propagation. Part i: Energy and energy flux. *Journal of Physical Oceanography*, *37*(7), 1829–1848. <https://doi.org/10.1175/jpo3085.1>
- Al-Shehhi, M. R., Song, H., Scott, J., & Marshall, J. (2021). Water mass transformation and overturning circulation in the Arabian Gulf. *Journal of Physical Oceanography*, *51*(11), 3513–3527. <https://doi.org/10.1175/jpo-d-20-0249.1>
- Andi, S., Hesari, A. R. E., & Farjami, H. (2020). Detection of internal waves in the Persian Gulf. *Remote Sensing Letters*, *12*(2), 190–198. <https://doi.org/10.1080/2150704x.2020.1847349>
- Buijsman, M. C., Uchiyama, Y., McWilliams, J. C., & Hill-Lindsay, C. R. (2012). Modeling semidiurnal internal tide variability in the southern California bight. *Journal of Physical Oceanography*, *42*(1), 62–77. <https://doi.org/10.1175/2011jpo4597.1>
- Cacchione, D. A., Pratson, L. F., & Ogston, A. S. (2002). The shaping of continental slopes by internal tides. *Science*, *296*(5568), 724–727. <https://doi.org/10.1126/science.1069803>
- Carter, G. S., Fringer, O., & Zaron, E. (2012). Regional models of internal tides. *Oceanography*, *25*(2), 56–65. <https://doi.org/10.5670/oceanog.2012.42>
- Carter, G. S., Merrifield, M. A., Becker, J. M., Katsumata, K., Gregg, M. C., Luther, D. S., et al. (2008). Energetics of M2 barotropic-to-baroclinic tidal conversion at the Hawaiian islands. *Journal of Physical Oceanography*, *38*(10), 2205–2223. <https://doi.org/10.1175/2008jpo3860.1>
- Devlin, A. T., Jay, D. A., Zaron, E. D., Talke, S. A., Pan, J., & Lin, H. (2017). Tidal variability related to sea level variability in the Pacific Ocean. *Journal of Geophysical Research: Oceans*, *122*(11), 8445–8463. <https://doi.org/10.1002/2017jc013165>
- Duda, T. F., & Rainville, L. (2008). Diurnal and semidiurnal internal tide energy flux at a continental slope in the south China sea. *Journal of Geophysical Research*, *113*(C3). <https://doi.org/10.1029/2007jc004418>
- Egbert, G. D., & Erofeeva, S. Y. (2002). Efficient inverse modeling of barotropic ocean tides. *Journal of Atmospheric and Oceanic Technology*, *19*(2), 183–204. [https://doi.org/10.1175/1520-0426\(2002\)019<0183:eimob>2.0.co;2](https://doi.org/10.1175/1520-0426(2002)019<0183:eimob>2.0.co;2)
- Egbert, G. D., & Ray, R. D. (2001). Estimates of m2 tidal energy dissipation from topeX/poseidon altimeter data. *Journal of Geophysical Research*, *106*(C10), 22475–22502. <https://doi.org/10.1029/2000jc000699>
- Eich, M. L., Merrifield, M. A., & Alford, M. H. (2004). Structure and variability of semidiurnal internal tides in Mamala Bay, Hawaii. *Journal of Geophysical Research*, *109*(C5). <https://doi.org/10.1029/2003jc002049>
- Fairall, C. W., Bradley, E. F., Hare, J. E., Grachev, A. A., & Edson, J. B. (2003). Bulk parameterization of air–sea fluxes: Updates and verification for the COARE algorithm. *Journal of Climate*, *16*(4), 571–591. [https://doi.org/10.1175/1520-0442\(2003\)016<0571:bpoasf>2.0.co;2](https://doi.org/10.1175/1520-0442(2003)016<0571:bpoasf>2.0.co;2)
- Gerkema, T., Lam, F. A., & Maas, L. R. (2004). Internal tides in the Bay of Biscay: Conversion rates and seasonal effects. *Deep Sea Research Part II: Topical Studies in Oceanography*, *51*(25–26), 2995–3008. <https://doi.org/10.1016/j.dsr2.2004.09.012>
- Guo, P., Fang, W., Liu, C., & Qiu, F. (2012). Seasonal characteristics of internal tides on the continental shelf in the northern south China sea. *Journal of Geophysical Research*, *117*(C4). <https://doi.org/10.1029/2011jc007215>

- Haigh, I. D., Pickering, M. D., Green, J. A. M., Arbic, B. K., Arns, A., Dangendorf, S., et al. (2020). The tides they are a-changin': A comprehensive review of past and future nonastronomical changes in tides, their driving mechanisms, and future implications. *Reviews of Geophysics*, 58(1). <https://doi.org/10.1029/2018rg000636>
- Jain, V., Shankar, D., Vinayachandran, P. N., Kankonkar, A., Chatterjee, A., Amol, P., et al. (2016). Evidence for the existence of Persian gulf water and red sea water in the Bay of Bengal. *Climate Dynamics*, 48(9–10), 3207–3226. <https://doi.org/10.1007/s00382-016-3259-4>
- Jithin, A., Francis, P., Unnikrishnan, A., & Ramakrishna, S. (2020). Energetics and spatio-temporal variability of semidiurnal internal tides in the Bay of Bengal and Andaman Sea. *Progress in Oceanography*, 189, 102444. <https://doi.org/10.1016/j.pocean.2020.102444>
- Jithin, A., Unnikrishnan, A., Fernando, V., Subeesh, M., Fernandes, R., Khalap, S., et al. (2017). Observed tidal currents on the continental shelf off the east coast of India. *Continental Shelf Research*, 141, 51–67. <https://doi.org/10.1016/j.csr.2017.04.001>
- Johns, W. E., Yao, F., Olson, D. B., Josey, S. A., Grist, J. P., & Smeed, D. A. (2003). Observations of seasonal exchange through the straits of Hormuz and the inferred heat and freshwater budgets of the Persian Gulf. *Journal of Geophysical Research*, 108(C12). <https://doi.org/10.1029/2003jc001881>
- Kämpf, J., & Sadrinasab, M. (2006). The circulation of the Persian gulf: A numerical study. *Ocean Science*, 2(1), 27–41. <https://doi.org/10.5194/os-2-27-2006>
- Kang, D., & Fringer, O. (2012). Energetics of barotropic and baroclinic tides in the Monterey Bay area. *Journal of Physical Oceanography*, 42(2), 272–290. <https://doi.org/10.1175/jpo-d-11-039.1>
- Kaur, H., Buijsman, M. C., Zhao, Z., & Shriver, J. F. (2024). Seasonal variability in the semidiurnal internal tide – A comparison between sea surface height and energetics. *Ocean Science*, 20(5), 1187–1208. <https://doi.org/10.5194/os-20-1187-2024>
- Kawamura, Y., Hayami, Y., Kohama, T., Kaneda, A., & Takeoka, H. (2006). Occasional intensification of semidiurnal internal tide in Bungo channel, Japan. *Geophysical Research Letters*, 33(14). <https://doi.org/10.1029/2006gl025866>
- Kelly, S. M., & Nash, J. D. (2010). Internal-tide generation and destruction by shoaling internal tides. *Geophysical Research Letters*, 37(23). <https://doi.org/10.1029/2010gl045598>
- Kunze, E., Rosenfeld, L. K., Carter, G. S., & Gregg, M. C. (2002). Internal waves in monterey submarine canyon. *Journal of Physical Oceanography*, 32(6), 1890–1913. [https://doi.org/10.1175/1520-0485\(2002\)032<1890:iwimsc>2.0.co;2](https://doi.org/10.1175/1520-0485(2002)032<1890:iwimsc>2.0.co;2)
- Large, W. G., McWilliams, J. C., & Doney, S. C. (1994). Oceanic vertical mixing: A review and a model with a nonlocal boundary layer parameterization. *Reviews of Geophysics*, 32(4), 363–403. <https://doi.org/10.1029/94rg01872>
- Leith, C. (1996). Stochastic models of chaotic systems. *Physica D: Nonlinear Phenomena*, 98(2–4), 481–491. [https://doi.org/10.1016/0167-2789\(96\)00107-8](https://doi.org/10.1016/0167-2789(96)00107-8)
- Liu, J., He, Y., Wang, D., Liu, T., & Cai, S. (2015). Observed enhanced internal tides in winter near the Luzon Strait. *Journal of Geophysical Research: Oceans*, 120(10), 6637–6652. <https://doi.org/10.1002/2015jc011131>
- Ma, J., Guo, D., Zhan, P., & Hoteit, I. (2021). Seasonal M2 internal tides in the Arabian Sea. *Remote Sensing*, 13(14), 2823. <https://doi.org/10.3390/rs13142823>
- MacKinnon, J. A., & Gregg, M. C. (2003). Mixing on the late-summer new England shelf—Solibores, shear, and stratification. *Journal of Physical Oceanography*, 33(7), 1476–1492. [https://doi.org/10.1175/1520-0485\(2003\)033<1476:motnle>2.0.co;2](https://doi.org/10.1175/1520-0485(2003)033<1476:motnle>2.0.co;2)
- Madah, F., & Gharbi, S. H. (2022). Numerical simulation of tidal hydrodynamics in the Arabian Gulf. *Oceanologia*, 64(2), 327–345. <https://doi.org/10.1016/j.oceano.2022.01.002>
- Marshall, J., Adcroft, A., Hill, C., Perelman, L., & Heisey, C. (1997). A finite-volume, incompressible Navier Stokes model for studies of the ocean on parallel computers. *Journal of Geophysical Research*, 102(C3), 5753–5766. <https://doi.org/10.1029/96jc02775>
- Masunaga, E., Arthur, R. S., Fringer, O. B., & Yamazaki, H. (2017). Sediment resuspension and the generation of intermediate nepheloid layers by shoaling internal bores. *Journal of Marine Systems*, 170, 31–41. <https://doi.org/10.1016/j.jmarsys.2017.01.017>
- Michael Reynolds, R. (1993). Physical oceanography of the Gulf, Strait of Hormuz, and the Gulf of Oman—Results from the Mt Mitchell expedition. *Marine Pollution Bulletin*, 27, 35–59. [https://doi.org/10.1016/0025-326X\(93\)90007-7](https://doi.org/10.1016/0025-326X(93)90007-7)
- Mooers, C. N. (1973). A technique for the cross spectrum analysis of pairs of complex-valued time series, with emphasis on properties of polarized components and rotational invariants. *Deep Sea Research and Oceanographic Abstracts*, 20(12), 1129–1141. [https://doi.org/10.1016/0011-7471\(73\)90027-2](https://doi.org/10.1016/0011-7471(73)90027-2)
- Müller, M. (2012). The influence of changing stratification conditions on barotropic tidal transport and its implications for seasonal and secular changes of tides. *Continental Shelf Research*, 47, 107–118. <https://doi.org/10.1016/j.csr.2012.07.003>
- Munk, W., & Wunsch, C. (1998). Abyssal recipes ii: Energetics of tidal and wind mixing. *Deep Sea Research Part I: Oceanographic Research Papers*, 45(12), 1977–2010. [https://doi.org/10.1016/s0967-0637\(98\)00070-3](https://doi.org/10.1016/s0967-0637(98)00070-3)
- Nash, J., Shroyer, E., Kelly, S., Inall, M., Duda, T., Levine, M., et al. (2012). Are any coastal internal tides predictable? *Oceanography*, 25(2), 80–95. <https://doi.org/10.5670/oceanog.2012.44>
- Niwa, Y., & Hibiya, T. (2004). Three-dimensional numerical simulation of M2 internal tides in the east China sea. *Journal of Geophysical Research*, 109(C4). <https://doi.org/10.1029/2003jc001923>
- Orlanski, I. (1976). A simple boundary condition for unbounded hyperbolic flows. *Journal of Computational Physics*, 21(3), 251–269. [https://doi.org/10.1016/0021-9991\(76\)90023-1](https://doi.org/10.1016/0021-9991(76)90023-1)
- Poul, H. M., Backhaus, J., Dehghani, A., & Huebner, U. (2016). Effect of subseabed salt domes on tidal residual currents in the Persian Gulf. *Journal of Geophysical Research: Oceans*, 121(5), 3372–3380. <https://doi.org/10.1002/2015jc011421>
- Pous, S., Carton, X., & Lazure, P. (2012). A process study of the tidal circulation in the Persian Gulf. *Open Journal of Marine Science*, 02(04), 131–140. <https://doi.org/10.4236/ojms.2012.24016>
- Pous, S. P., Carton, X., & Lazure, P. (2004). Hydrology and circulation in the Strait of Hormuz and the gulf of Oman—results from the GOGP99 experiment: 1. Strait of Hormuz. *Journal of Geophysical Research C: Oceans*, 109(C12). <https://doi.org/10.1029/2003JC002145>
- Reynolds, R. M. (1993). Physical oceanography of the Gulf, Strait of Hormuz, and the Gulf of Oman—results from the Mt Mitchell expedition. *Marine Pollution Bulletin*, 27, 35–59. [https://doi.org/10.1016/0025-326X\(93\)90007-7](https://doi.org/10.1016/0025-326X(93)90007-7)
- Salim, M., Subeesh, M. P., Scott, J., Song, H., Marshall, J., & Alshehhi, M. R. (2024). Role of tidal mixing on ocean exchange through the Strait of Hormuz. *Environmental Research Communications*, 6(7), 071006. <https://doi.org/10.1088/2515-7620/ad578c>
- Sharples, J., Moore, C. M., Hickman, A. E., Holligan, P. M., Tweddle, J. F., Palmer, M. R., & Simpson, J. H. (2009). Internal tidal mixing as a control on continental margin ecosystems. *Geophysical Research Letters*, 36(23). <https://doi.org/10.1029/2009gl040683>
- Shaw, P., Ko, D. S., & Chao, S. (2009). Internal solitary waves induced by flow over a ridge: With applications to the northern south China sea. *Journal of Geophysical Research*, 114(C2). <https://doi.org/10.1029/2008jc005007>
- Smith, W. H. F., & Sandwell, D. T. (1997). Global sea floor topography from satellite altimetry and ship depth soundings. *Science*, 277(5334), 1956–1962. <https://doi.org/10.1126/science.277.5334.1956>

- Subeesh, M. P., & Unnikrishnan, A. (2016). Observed internal tides and near-inertial waves on the continental shelf and slope off Jaigarh, central west coast of India. *Journal of Marine Systems*, 157, 1–19. <https://doi.org/10.1016/j.jmarsys.2015.12.005>
- Subeesh, M. P., Unnikrishnan, A., Fernando, V., Agarwadekar, Y., Khalap, S., Satelkar, N., & Sheno, S. (2013). Observed tidal currents on the continental shelf off the west coast of India. *Continental Shelf Research*, 69, 123–140. <https://doi.org/10.1016/j.csr.2013.09.008>
- Subeesh, M. P., Unnikrishnan, A., & Francis, P. (2021). Generation, propagation and dissipation of internal tides on the continental shelf and slope off the west coast of India. *Continental Shelf Research*, 214, 104321. <https://doi.org/10.1016/j.csr.2020.104321>
- Swift, S. A., & Bower, A. S. (2003). Formation and circulation of dense water in the Persian/Arabian Gulf. *Journal of Geophysical Research C: Oceans*, 108(C1). <https://doi.org/10.1029/2002jc001360>
- Tanaka, Y. (2024). Superinertial internal tides propagating along the coast: Dynamics and energetics revealed through topographic modes. *Journal of Physical Oceanography*, 54(11), 2321–2336. <https://doi.org/10.1175/jpo-d-23-0210.1>
- Xu, Z., Wang, Y., Liu, Z., McWilliams, J. C., & Gan, J. (2021). Insight into the dynamics of the radiating internal tide associated with the kuroshio current. *Journal of Geophysical Research: Oceans*, 126(6). <https://doi.org/10.1029/2020jc017018>
- Yan, T., Qi, Y., Jing, Z., & Cai, S. (2020). Seasonal and spatial features of barotropic and baroclinic tides in the northwestern south China sea. *Journal of Geophysical Research: Oceans*, 125(1). <https://doi.org/10.1029/2018jc014860>
- Zhao, Z. (2021). Seasonal mode-1 M2 internal tides from satellite altimetry. *Journal of Physical Oceanography*. <https://doi.org/10.1175/jpo-d-21-0001.1>
- Zhao, Z., & Qiu, B. (2023). Seasonal west-east seesaw of M2 internal tides from the Luzon Strait. *Journal of Geophysical Research: Oceans*, 128(3). <https://doi.org/10.1029/2022jc019281>
- Zilberman, N. V., Becker, J. M., Merrifield, M. A., & Carter, G. S. (2009). Model estimates of M2 internal tide generation over mid-Atlantic ridge topography. *Journal of Physical Oceanography*, 39(10), 2635–2651. <https://doi.org/10.1175/2008jpo4136.1>